Effect of Wind on Self-Audition of Human Voice

Rapolas Daugintis

School of Electrical Engineering

Thesis submitted for examination for the degree of Master of Science in Technology.
Espoo 22.7.2021

Supervisor

Prof. Ville Pulkki

Advisor

Dr Timo Lähivaara

Aalto University
School of Electrical
Engineering

Aalto University
School of Electrical
Engineering

Aalto University, P.O. BOX 11000, 00076 AALTO
www.aalto.fi
Abstract of the master's thesis

Author Rapolas Daugintis

Title Effect of Wind on Self-Audition of Human Voice

Degree programme Computer, Communication and Information Sciences

Major Acoustics and Audio Technology **Code of major** ELEC3030

Supervisor Prof. Ville Pulkki

Advisor Dr Timo Lähivaara

Date 22.7.2021 **Number of pages** 62+1 **Language** English

Abstract

During one's speech, the human auditory system continuously monitors one's own voice and subconsciously adjusts it based on the way it is heard. Part of the sound produced in the human vocal tract radiates from the mouth, propagates in the air around the head, and reaches the ears externally. It is therefore affected by the background air conditions, such as the wind, which, in turn, may impact the way one hears oneself.

This thesis investigates the influence of wind around the human head on the sound propagation from the mouth to the ears. The effect is examined using computer simulations and measurements. The simulations, which are limited to a two-dimensional horizontal cross-section of a model head, are implemented using finite element numerical methods in COMSOL Multiphysics® software. The background airflow around the head is modelled using the RANS-based SST turbulence model, and the simulated background flow parameters are used in a linearised Navier-Stokes aeroacoustics simulation. The measurements are conducted on a cylindrical measurement rig with a loudspeaker and microphones attached. The rig is placed on the roof of a moving van to imitate a horizontal airflow around a cross-section of the human head. The effect is studied for wind speeds from 6 m/s to 24 m/s in the upwind (incident on the face) and downwind (incident on the back) directions.

Simulation and measurement results demonstrate that sound radiated from the position of the mouth to the location of the ears is attenuated in the upwind scenario and amplified in the downwind case. The amplification and attenuation depend on the wind speed, so the effect is most prominent in the fastest winds studied. It also depends on the sound frequency: the lowest frequencies are impacted the most (within a few decibel range), while the difference vanishes in the higher frequencies (from around 1–4 kHz in the simulations and measurements presented). The results are in line with previous theoretical and empirical descriptions of the upstream amplification phenomena. The effect might influence the perceived loudness of the fundamental frequency of one's own voice and the first formants of the phonemes, which are essential properties of human speech.

Keywords aeroacoustics, fluid dynamics, sound in background flow, voice in wind, hearing one's own voice

Preface

The research work for this thesis was carried out at the Aalto Acoustics Lab. I want to thank my supervisor, Prof. Ville Pulkki, for the opportunity to work on this intriguing topic and participate in the everyday life of the lab and for his support throughout the research process. I am also grateful to Dr Timo Lähivaara for his guidance on the intricacies of the computer simulations and Aleksi Öyry for his dedicated hand when preparing and conducting the measurements. Furthermore, I am thankful to Helsinki city authorities for allowing access to the Helsinki-Malmi airport runaway in the name of the 'Great Science'.

I am extending my gratitude to everyone in the lab for numerous on- and off-topic conversations about all things sound. Special thanks go to my coursemates Mike and Janis for the mutual support we gave each other during the socially distanced and isolating times.

Finally, worthy of recognition are the rising desks and monitors in the lab for keeping my posture (somewhat) intact, the lab's coffee machine for the thesis ink, Olarin Panimo for the supply of Thursday beverages, my bike for its unwavering support throughout the informal 'shouting in the wind' experiments, and the nature in Helsinki for keeping me sane.

Otaniemi, 22.7.2021

Rapolas Daugintis

Contents

Symbols and abbreviations

Symbols

c	speed of sound
D	length scale (e.g. diameter)
$\mathbf{F}$	force
$\mathbf{g}$	gravitational acceleration
i	imaginary number; arbitrary index
$\mathbf{I}$	identity matrix
j	arbitrary index
k	turbulent kinetic energy
L	sound level
$\mathbf{M}$	mass source
M	Mach number
N	number of measurement segments
p	fluid pressure
Re	Reynolds number
t	time
$\mathbf{u}$	fluid velocity
u	fluid speed (magnitude of fluid velocity)
x	first spatial dimension
y	second spatial dimension
ϵ	turbulent dissipation rate
μ	dynamic viscosity
μ_B	bulk viscosity
μ_t	turbulent viscosity
ν	kinematic viscosity
ρ	fluid density
ϕ	grazing angle
ψ	basis and test functions in FEM
ω	angular frequency; specific dissipation rate
Ω	fluid domain
$\partial\Omega$	boundary of fluid domain

Operators

$\mathbf{a}$	vector variable
$\mathbf{a}^\top$	transpose of $\mathbf{a}$
a	scalar variable, magnitude of vector variable $\mathbf{a}$
$\overline{a}$	mean of variable a
a_0	background flow variable a
a'	turbulent variation of a around the mean
$\tilde{a}$	acoustic perturbation of a around the mean
a_h	discrete approximation of a
σ_a	standard deviation of variable a
$\sigma_{\overline{a}}$	standard error of the mean of variable a
$\mathbf{a} \cdot \mathbf{b}$	scalar product of $\mathbf{a}$ and $\mathbf{b}$
$\mathbf{a} \otimes \mathbf{b}$	outer product of $\mathbf{a}$ and $\mathbf{b}$
Δ	difference
$\boldsymbol{\nabla}$	gradient operator
$\boldsymbol{\nabla} \cdot$	divergence operator
$\mathbf{a} \cdot \boldsymbol{\nabla}$	convective operator
∇^2	Laplace operator
$\dfrac{\partial}{\partial t}$	partial derivative with respect to variable t
$\dfrac{\mathrm{D}}{\mathrm{D}t}$	material derivative with respect to variable t
$\sum_i$	sum over index i

Abbreviations

CF	crest factor
CFD	computational fluid dynamics
DAW	digital audio workstation
FEM	finite element method
FFT	fast Fourier transform
IR	impulse response
LNS	linearised Navier-Stokes equations
NS	Navier-Stokes equations
PML	prefectly matched layer
RANS	Reynolds-averaged Navier–Stokes equations
RMS	root mean square
SEM	standard error of the mean
SNR	signal-to-noise ratio
SPL	sound pressure level
SST	Menter's Shear Stress Transport turbulence model

1 Introduction

The importance of the human voice as a means of communication and self-expression is indisputable amongst the population with normal hearing. A crucial part of vocal communication is the ability to monitor one's own speech in order to assess its accuracy and optimise it for the existing conditions. Such a monitoring process happens through the human hearing mechanism. In contrast to when one listens to external sources, internal sound from the vocal folds is transmitted along two paths to reach the inner ear. When externally radiated from the mouth, the voice propagates through the air, reaching the outer ear. It is then registered by the hearing mechanism similarly as with any other external sound. However, the sound also travels internally from the vocal folds, through the bone and human tissue, directly reaching the inner ear. The research into the balance between the two paths forms part of the seminal compendium of 'Experiments in Hearing' by von Békésy [1]. While the internal bone-and-tissue-conducted sound transmission path is unaffected by the external conditions, the air-conducted path is subject to them. Therefore, changes in the external conditions affect the quality of self-audition and, in turn, may result in changes to the voice production.

One example of the psychoacoustic effect of external sonic conditions on human voice production is the Lombard effect, which has already been studied for more than a hundred years [2]. According to the studies, speech is subconsciously adapted by changing its features, primarily by raising its level (loudness), in the presence of the background noise. However, despite the lengthy research conducted on this phenomenon, the investigation into different external causes of the change in the ability to hear oneself *per se* has not been comprehensive. One overlooked cause has been the effect of wind around the human head on the external airborne voice radiation path.

Typically, the influence of wind on sound propagation is a well-researched topic in the context of environmental noise [3]–[5] and, more generally, aeroacoustics [6]. The wind is one of the considerations in the practice of mapping the environmental noise, a process used to assess the environmental noise impact of new or existing developments (such as roads, rail, and industrial plants) on the surrounding residential and ecological areas. Therefore, the wind conditions are addressed when developing common noise mapping methodologies, such as CNOSSOS-EU [7] or Nord2000 [8]. On a broader scale, the field of aeroacoustics is concerned with the induction and interaction of sound waves and air motion. The most common areas of interest in aeroacoustics are high-speed transportation (for example, aeroplanes [9] or trains [10], [11]) as well as wind turbine noise [12], [13]. This type of research encompasses the sound generation by air interacting with the moving surfaces and the effect of air motion on the outward propagation of sound from the object. However, the effects of smaller scale and lower airflow velocities on the sound waves have been largely omitted from the main corpus of aeroacoustics research.

Recently, the effect of wind on the directivity of the human voice has been investigated [14], [15] leading to some noticeable findings. However, the research focused on the sound path emanating outwards from the speaker. Thus, the sound

levels were modelled and measured some distance away from the source. This thesis serves to continue this research and investigates the local sound propagation around the sound source (the speaker).

The main goal of this study is to determine the effect of the direction and strength of wind around the human head on the external propagation path the sound takes from the mouth to the ears and its result on the ability to hear one's own voice. To achieve this objective, the thesis presents and compares the results from computer simulations and measurements of a cross-section of the human head in the wind. Due to the complexity of the model, the simulation is constrained to a two-dimensional system; hence, the discussion of wind direction is limited to the horizontal plane. In addition to serving as a theoretical investigation aimed at deepening the human understanding of acoustic phenomena, this study might find utility in further development of audio technology, for instance, in the context of wearable audio devices or virtual reality applications.

The rest of this thesis is divided into six chapters. Chapter 2 overviews the relevant theoretical background. It is subdivided by topics on general aerodynamics, physics of sound, the human voice, and the human hearing mechanism. Chapters 3 and 4 describe modelling and measurement methodologies, respectively. Chapter 5 presents modelling and measurement results, then discusses and compares the two. Finally, Chapter 6 summarises the research, its key findings, limitations, and potential future directions.

2 Background

From the physics perspective, *sound* can be defined as mechanical perturbations around the equilibrium state, propagating within elastic material medium [16]. Therefore, the field of acoustics is contingent upon broader principles governing the physics of the propagation media. The relevant material of interest for the study on voice propagation around the human head is air. Composed of a mixture of gases, the air is generally considered under a broader category of fluids. *Fluid* is defined as a phase of matter, which continuously transforms (flows) under applied stress [17]. The underlying laws of fluid mechanics thus have a direct effect on the propagation of sound in air. To provide the theoretical context that the thesis work is built upon, the background chapter presents the fundamental concepts used to describe fluid dynamics and aerodynamics (a subset of fluid dynamics, which describes air movement) and then discusses the physics of sound in air.

Furthermore, the topic of this thesis deals with human voice production and hearing mechanisms. Therefore, the subsequent sections of this chapter also overview the production of speech and human hearing.

2.1 Fundamentals of fluid dynamics

2.1.1 Navier-Stokes equations of fluid flow

One of the key equations, which describe a Newtonian fluid behaviour, is the Navier-Stokes (NS) momentum equation:

$$\rho\left(\frac{\partial \mathbf{u}}{\partial t}+\mathbf{u}\cdot\boldsymbol{\nabla}\mathbf{u}\right)=-\boldsymbol{\nabla}p+\boldsymbol{\nabla}\cdot\left(\mu\left(\boldsymbol{\nabla}\mathbf{u}+(\boldsymbol{\nabla}\mathbf{u})^{\top}\right)-\frac{2}{3}\mu(\boldsymbol{\nabla}\cdot\mathbf{u})\mathbf{I}\right)+\mathbf{F}. \tag{1}$$

The complete derivation of the equation is presented in fluid mechanics textbooks (e.g. [18]–[20]). In its essence, the equation represents Newton's second law (i.e. force is equal to the product of mass and acceleration) for a unitary fluid element. In this equation, ρ is the fluid density, $\mathbf{u}$ is the flow velocity vector, p is pressure, μ is the dynamic viscosity. Finally, $\mathbf{I}$ is the identity matrix, and vector $\mathbf{F}$ represents the net external force applied to the fluid.

From a conceptual point of view, Equation 1 can be broken down into several components. The left-hand side represents the acceleration of the unitary fluid parcel. The sum of temporal and convective velocity derivatives is known as the material derivative

$$\frac{\partial \mathbf{u}}{\partial t}+\mathbf{u}\cdot\boldsymbol{\nabla}\mathbf{u}\equiv\frac{\mathrm{D}\mathbf{u}}{\mathrm{D}t} \tag{2}$$

and corresponds to the rate of change of flow velocity (i.e. acceleration) of a fluid parcel as the parcel moves along the flow.

On the right-hand side of the equation, three contributing force components can be identified. The first contribution comes from the negative pressure gradient. It can be intuitively recognised that in the presence of high- and low-pressure zones, the fluid flows from the high pressure to the low pressure, i.e. against the pressure gradient.

The second term on the right-hand side corresponds to the viscous forces within the fluid. Viscosity describes a fluid's resistance to deform, so fluids with high viscosity (e.g. honey) flow slowly while the ones with low viscosity (e.g. air) flow easily. Dynamic viscosity coefficient μ, used in the equations, is the constant of proportionality, which links the gradient of flow velocity along the direction, perpendicular to the flow direction, and shear stress, exerted along the direction of flow [20, p. 936]. For Newtonian fluids, this proportionality is linear. The NS equation presented above uses a simplification, in which mechanical and thermodynamic pressure is assumed to be the same. The second viscosity coefficient (a.k.a. bulk or volume viscosity) is therefore expressed in terms of dynamic viscosity and thus removed from the equation. Evidence shows that bulk viscosity coefficient is relevant in shock waves and sound-wave attenuation, but the effect is considered minor in most cases of fluid flow [21, p. 67].

Viscosity in the fluid is caused by the internal interactions of molecules, therefore, the viscosity of air is much lower than that of a liquid due to the large distances between the molecules in gases. Free air flow could be modelled as inviscid (i.e. having zero viscosity); however, even small viscous forces become critical when resolving the flow close to surfaces (as initially indicated by d'Alembert's Paradox, which predicted non-physical zero drag for a cylinder in air flow due to unaccounted viscous boundary effects [22]).

The rightmost term in the NS momentum equation is the external net force component. In the absence of any other external forces apart from gravity, the latter force term is sometimes replaced by an expression $\rho\mathbf{g}$.

The second essential equation in fluid mechanics, which forms the set of NS equations, is the continuity equation:

$$\frac{\partial \rho}{\partial t} + \boldsymbol{\nabla} \cdot (\rho \mathbf{u}) = 0. \tag{3}$$

The equation is derived from the conservation of mass (complete derivation is presented in, e.g. [19, pp. 84–86]). The equation illustrates that the temporal change of the mass within a given fluid parcel has to correspond to the net rate at which the matter leaves or enters the parcel.

So far, the presented equations were applicable to all compressible and viscous fluids. Gasses, including air, are generally treated as compressible (their density changes with pressure). However, for speeds lower than 100 m/s or, in other words, for Mach numbers (which is defined as the ratio between the speed of flow and the speed of sound) $M < 0.3$, the relative pressure changes due to the flow are small compared to the absolute atmospheric pressure (relative variation of density is less than 5% [20, Ch. 8.5]). Therefore, for wind around a human head, the air can be treated as incompressible, greatly simplifying the equations of fluid motion. On the other hand, sound is a pressure wave, which relies on the compressibility of the medium [23, p. 13]. Thus, the concept of compressible flow will be revisited in the following sections on the sound waves.

Under the assumption of incompressible flow, both the temporal and the spatial

derivatives of density are zero, thus the continuity equation can be simplified to:

$$\boldsymbol{\nabla} \cdot \mathbf{u} = 0. \tag{4}$$

Using this result and assuming negligible temperature variations and thus constant viscosity μ [19, p. 104], NS equation can also be simplified:

$$\rho \left(\frac{\partial \mathbf{u}}{\partial t} + \mathbf{u} \cdot \boldsymbol{\nabla} \mathbf{u} \right) = -\boldsymbol{\nabla} p + \mu \nabla^2 \mathbf{u} + \mathbf{F} \tag{5}$$

Although conceptually solid and based on fundamental laws of classical mechanics, the NS equations present a challenge to theoreticians to this day. It is still to be proved that smooth (continuously differentiable) solutions always exist to the NS equations given a set of arbitrary initial conditions. Despite these fundamental uncertainties, the NS equations serve as a vital tool in simulating the underlying physics of numerous fields.

2.1.2 Turbulence

The fluid flow has two modes: laminar and turbulent. When the viscous forces dominate in the fluid, the flow is said to be laminar. In such cases, the flow tends to be regular: fluid particles travel along parallel paths with little mixing (convection) perpendicular to the fluid flow. However, if the flow's kinetic energy is strong enough to overcome the viscous interaction effects, the flow becomes irregular, chaotic, and unpredictable. Such flow is called turbulent and can be characterised by its randomness, nonlinearity, diffusivity, vorticity (flow forms eddies of various sizes and particles mix along various length and time scales) and dissipation of energy [19, p. 538].

The emergence of a chaotic turbulent motion is caused by the non-linear factors of the NS equation. The convective acceleration term ($\mathbf{u} \cdot \boldsymbol{\nabla} \mathbf{u}$) produce a range of harmonic scale structures for a given set of initial conditions. At the same time, the estimation of pressure field at one point is subject to the fluid state at every other point. [24, Ch. 1.3] provides an overview and intuition behind these non-linear terms. The result of the non-linearities is turbulent flow's susceptibility to initial conditions. Furthermore, the behaviour of the turbulent motion is conditioned by the dimensionality of the system: energy dissipation in a three-dimensional turbulent flow is different from a two-dimensional one due to constraints on vorticity [25]. Hence, it is problematic to predict the turbulent flow for more extended time scales and complex geometries.

The transition line between the two modes of flow is not definite since the turbulence needs space and time to develop. However, the existence of turbulence in the flow can be estimated by the Reynolds number of the system:

$$Re = \frac{\rho u D}{\mu} = \frac{u D}{\nu} \tag{6}$$

where ρ is the density of the fluid, u is the flow speed, D is the length scale of the system, and μ is the dynamic viscosity of the fluid (sometimes, the Reynolds number

is expressed in terms of kinematic viscosity $\nu = \mu/\rho$). Conceptually, the numerator of the expression represents the inertial forces and the denominator — viscous forces; thus, the Reynolds number denotes the ratio between the two. The measurement of the length scale D depends on the system in question. In the case of external flow, it is typically the diameter of a cylinder or a sphere surrounded by the flow. It can be seen in practice that for a flow around a circular cylinder (which could be used to represent a simplified head model), the transition to turbulence occurs for $Re \sim 10^5$ [20, Sec. 3.18]. However, the limit is not distinct and can depend on an individual system [24, pp. 5–6].

2.1.3 Turbulence models

One way of predicting turbulent flows is by using a statistical approach. Variables such as pressure and velocity can be treated as random variables. Provided the random fluctuations are small compared to their absolute mean, one can express these values as a superposition of the mean with respect to time and a stochastic variation around it (e.g. $u = \overline{U} + u'$ and $p = \overline{P} + p'$). Such expressions can be substituted into the NS equations (Equations 4 and 5, assuming incompressible case for simplicity) and the equations averaged in time. The resulting equations are called Reynolds-averaged Navier–Stokes equations (RANS), and they are used in many computer fluid dynamics (CFD) applications. The full derivations of RANS are given in textbooks (e.g. [24, Sec. 2.2.2], [18, Sec. 7.2], [19, Ch. 13]), where several rules of averaging have to be applied to reach the resulting equations. In a vectorised form, the incompressible RANS momentum equation can be expressed as:

$$\frac{\mathrm{D}\rho\overline{\mathbf{U}}}{\mathrm{D}t} + \boldsymbol{\nabla} \cdot \left(\rho\overline{\mathbf{u}' \otimes \mathbf{u}'}\right) = -\boldsymbol{\nabla}\overline{P} + \mu\nabla^2\overline{\mathbf{U}} + \mathbf{F} \tag{7}$$

where $\mathbf{u}' \otimes \mathbf{u}' = u_i' u_j'$ (in index notation) is the outer product. Depending on the formalism used, the exact form of the equation might vary, but the most important feature (and a challenge) of the RANS model is the term $\rho\overline{u_i' u_j'}$, known as the Reynolds stress tensor. The diagonal terms of the tensor ($i = j$), where the velocity components along each orthogonal direction are squared, correspond to the mean turbulent kinetic energy [24, p. 39]. However, the off-diagonal terms of this nonlinear tensor are non-zero too, due to the cross-correlation between the orthogonal velocity components (i.e. $\overline{u_i' u_j'} \neq 0$ even when $i \neq j$), caused by the anisotropic nature of turbulence [19, pp. 551–552]. There are no analytical equations for the components of the Reynolds tensor, hence the RANS equations on their own cannot be closed.

A few different approaches are used in current-day CFD modelling to close the system of equations. They all rely on several assumptions, while the existence and form of exact analytic solution to the equations are still unknown. The Boussinesq hypothesis [24, Sec. 2.5] is a popular approximation used in multiple turbulent models. It uses the analogy from viscous stress and defines a new quantity, called turbulent viscosity μ_t. Reynolds tensor is then expressed as a mean strain rate, scaled by μ_t, similarly to how dynamic viscosity is defined. However, contrary to μ, which is a property of the material, μ_t depends on the properties of the flow [19,

p. 581]. The Boussinesq model shifts the problem away from Reynolds tensor but still leaves the turbulent (a.k.a. eddy) viscosity unknown.

Additional models were developed to find the expression for turbulent viscosity. A popular one, presented in [26], is $k-\epsilon$ model, which expresses μ_t in terms of turbulent kinetic energy k and turbulent dissipation rate ϵ. The latter term describes the speed at which the turbulent kinetic energy is converted to thermal energy due to the viscous forces. These two quantities are found by solving two transport equations (i.e. equations that govern the transformation of a quantity w.r.t. movement in space), which involve several empirically determined constants. Although widely used, the model is inaccurate in predicting flows close to the boundary when the pressure gradients are adverse [27, p. 228]. Another two-equation model, called $k-\omega$, aims to overcome this limitation. It uses a specific dissipation rate ω, representing the dissipation rate ϵ scaled by turbulent kinetic energy k. It also uses two transport equations with a different set of empirical constants to find the two variables. The most contemporary variation of equations is presented in [27, Sec. 4.3.1.]. The $k-\omega$ model resolves the flow close to the boundary more accurately; however, the model result is sensitive to the turbulence parameters chosen for free-stream flow, with even minor alterations affecting the simulated flow close to the boundary [28]. A hybrid model was therefore proposed in [29], which uses a blending function to switch between a $k-\omega$ model close to the boundaries and $k-\epsilon$ model in the free-stream case. In its complete form, the model, known as the Menter's Shear Stress Transport (SST) model, combines the stability of $k-\epsilon$ model with respect to the free-stream turbulence parameters and the accuracy of $k-\omega$ close to the boundary. It is, therefore, a widely used model to close the RANS equations and predict the fluid flow.

2.1.4 Boundary layers

At the interface between the fluid and the solid, the fluid motion is subject to boundary conditions. Fluid particles closest to the stationary boundary interact with the solid surface particles, lose their kinetic energy, and are thus slowed down (or sped up if the surface is moving). The first layer of the fluid particles, which borders the solid surface, is assumed to adhere to the solid surface and move with the same velocity as the solid (or be stationary), forming a *no-slip* boundary condition. In the reference frame of the solid boundary $\partial\Omega$, which bounds the fluid domain Ω, this condition can be represented by a Dirichlet boundary condition $\mathbf{u}(\partial\Omega) = 0$.

Due to the viscous fluid particle interactions, the influence of the boundary condition on the flow velocity propagates across the subsequent parallel layers of the fluid flow. The resulting velocity profile close to the boundary is schematically represented in Figure 1a. The region close to the boundary, where the flow velocity is affected (typically defined up to the point where the flow velocity reaches 99% of the freestream velocity [30, p. 30]) is known as the boundary layer.

Boundary layer theory, developed by Prandtl as a way to resolve the d'Alembert's paradox [30, pp. XXI–XXV], states that high Reynolds number flow can be divided into two regions: the wider freestream region, where the viscous effects can be ignored,

and the thin boundary layer, characterised by the gradients of flow parameters with respect to the distance away from the boundary due to fluid viscosity [30, p. 29]. The thickness and the form of the boundary layer are dependent on the Reynolds number, and at the two extremes, the boundary layer can be categorised as laminar or turbulent. For a flow parallel to the boundary surface, any laminar boundary layer transitions to a turbulent boundary layer after a certain critical distance [30, p. 33]. Compared to the laminar boundary layer, where only the viscosity governs the flow velocity gradient, the turbulent boundary layer is subdivided into much thinner viscous and larger turbulent sublayers. For the flow in the latter sublayer, the viscosity effects are negligible compared to the 'apparent' friction due to random turbulent flow fluctuations [30, p. 35].

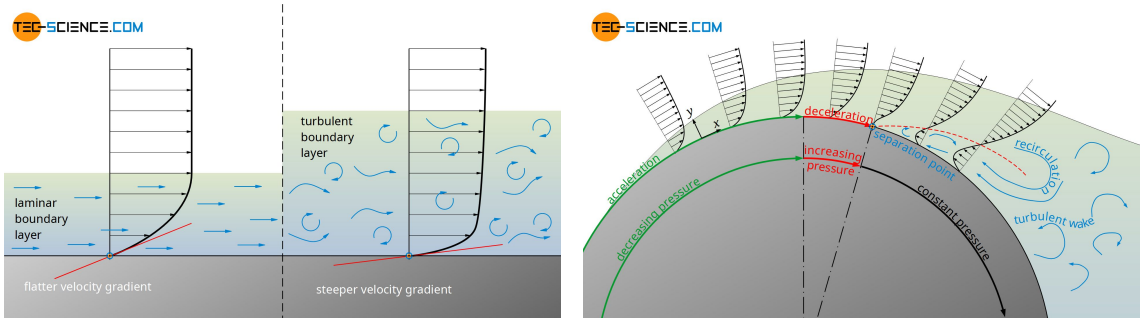

(a) *Laminar versus turbulent boundary layers.* (b) *Flow around a cylinder.*

Figure 1: *Examples of boundary layer flow. Figures reproduced with permission from [31].*

2.1.5 Flow around a cylinder

The behaviour of wind around a human head could be qualitatively described using a simplified case of flow around a cylinder. Such a system can be solved analytically, and it offers a good indication of the flow behaviour around more complex geometries.

The flow profile around a cylinder strongly depends on the Reynolds number. As summarised in [30, Tab. 1.1], at vanishing Reynolds numbers, the creeping flow is steady and symmetric. As Re increases, a *wake region* starts developing in the downstream direction with a recirculating flow. Further incremental changes lead to more unstable flow in the wake until the critical regime is reached and turbulence comes into effect. The thin layer between the wake region and the surrounding freestream flow is called the *shear layer*, and it is characterised by steep flow velocity gradients perpendicular to the mean flow direction.

Figure 1b schematically shows the development of the boundary layer and the wake region for flow around a cylinder in the turbulent regime. Initially, on the incident side of the body, the flow accelerates as pressure is converted into kinetic energy. After reaching the widest cross-sectional point of the obstacle, the flow starts slowing down, and the pressure increases due to energy conservation. At the *separation point*, the particles closest to the surface in the boundary layer, affected

by friction, cannot overcome the pressure build-up. Their motion is stopped and reversed, and a recirculating vortex is formed, which propagates downstream along a turbulent wake [30, Sec. 2.6].

The wind speeds of interest for this thesis are within a range of 6 m/s to 24 m/s, covering the wind strengths from moderate breeze to strong gale [32]. For a circle corresponding to a cross-section of a model head, its diameter is around 0.2 m. The kinematic viscosity of air is approximately $1.5 \times 10^{-5}\,\mathrm{m^2/s}$ at 20 °C [33]. Therefore, for the wind speed of $\sim 10\,\mathrm{m/s}$, the Reynolds number of the system is approximately:

$$Re = \frac{uD}{\nu} \approx \frac{10\,\mathrm{m/s} \times 0.2\,\mathrm{m}}{1.5 \times 10^{-5}\,\mathrm{m^2/s}} = 1.3 \times 10^5. \tag{8}$$

At these wind speeds, the flow regime is categorised as subcritical or critical (critical regime starts at $Re > 10^5$). Therefore, flow separation and turbulent wake region are prominent features in the system of interest.

2.2 Physics of sound

Typically, sound generation and propagation are considered in homogeneous media (air) at rest. The standard formulation of acoustic wave equation:

$$\frac{1}{c^2}\frac{\partial^2 \tilde{p}}{\partial t^2} = \nabla^2 \tilde{p} \tag{9}$$

where $\tilde{p}$ is acoustic pressure perturbation and c is the speed of sound (approx. 343 m/s in 20 °C air), is derived from an inviscid flow assumption, which simplifies the Navier-Stokes equation (1) to Euler equation by setting $\mu = 0$. Together with the continuity equation and the thermodynamic equation of state for the ideal gas, these expressions are linearised by assuming small linear time-varying acoustic perturbations around static variables and ignoring vanishing second-order terms (full derivation is presented in, e.g. [34, Ch. 2]). However, if the effect of non-uniform background flow has to be considered, the linear acoustic wave equation cannot incorporate such effects; thus, a more complex description has to be used for the acoustic wave behaviour.

2.2.1 Sound propagation in background flow

In a simplified scenario, in which a stationary source emits the sound into a medium of uniform flow (e.g. uniform wind in the air), the speed of the sound wave, recorded by a stationary observer, is a superposition of the velocity of sound in the medium and the velocity of the background flow. Therefore, the sound, which propagates against the flow direction, has its effective speed reduced, while the one propagating along the flow is sped up by the flow. The wave equation for the sound in uniform flow can be derived for the coordinate system at rest by using the Galilean coordinate transformation from the system in motion [34, p. 30]. The resulting wave equation has an additional convective term, which arises from the time derivative transformation (derivation given in [35, Sec. 11.1]):

$$\frac{1}{c^2}\left(\frac{\partial}{\partial t} + \mathbf{u}_0 \cdot \boldsymbol{\nabla}\right)^2 \tilde{p} = \nabla^2 \tilde{p} \tag{10}$$

where $\mathbf{u}_0$ is the background flow velocity.

The background motion of the sound waves leads to a frequency shift if the comoving receiver records the sound as opposed to the stationary one. This effect, known as the Doppler effect, alters the frequency by a factor of $M = u_0/c$ (the Mach number) and depends on the flow direction. It is caused by the difference in the observed (effective) speed of sound by the two receivers, while the observed sound wavelength remains the same (a thorough explanation is given in, e.g. [35, pp. 699–700] and [34, pp. 259–262]).

For a stationary source, which radiates sound into the moving fluid, the energy of its acoustic waves is also affected by the velocity of the background flow. It was shown in [36] that a plane wave radiated into a narrow tube is amplified in the upstream direction (when propagating against the flow) and attenuated in the downstream direction. The amplification factor appears to depend on the Reynolds regime of the flow. For low-Mach flow regimes ($M < 0.1$) in the duct, the pressure amplification factor for the upstream versus the downstream flow follows a $(1+M)^2/(1-M)^2$ trend line. For example, a 12 m/s flow would result in a 1.2 dB amplification for the plane wave, propagating upstream in the duct as opposed to downstream. Reciprocally, a convective amplification happens when a sound source moves in a stationary medium [37]. As explained in [34, pp. 265–266], energy exchange occurs between the sound waves and the mean flow through nonlinear mean momentum flux when the sound waves encounter a sheared background flow. When sound waves enter the region of opposing flow, the energy is transferred from the mean flow to the acoustic waves. The opposite energy exchange happens for the waves, which enter the region of downstream flow: they get attenuated.

When the wavelength of the sound is smaller than the length scale of the system (e.g. sizes of the obstacles or flow interfaces), the wave propagation can be approximated by rays, which are perpendicular to the sound wavefronts. At the interface between two media, which are moving at different velocities (i.e. a simplified shear

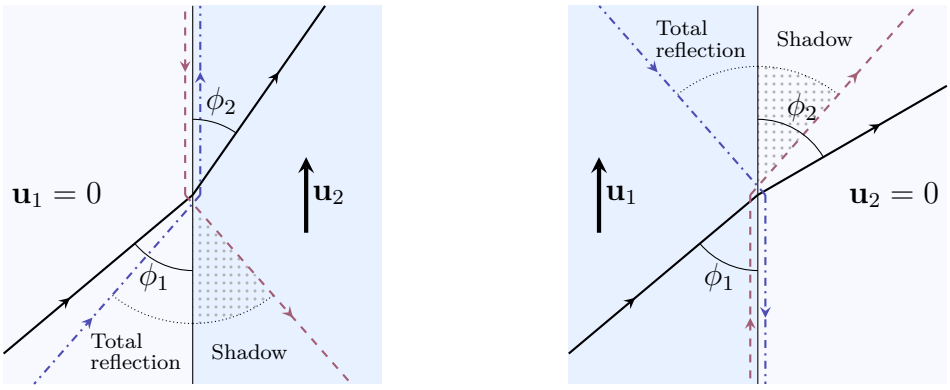

(a) $\Delta\mathbf{u} > 0$, $\phi_1 > \phi_2$. (b) $\Delta\mathbf{u} < 0$, $\phi_1 < \phi_2$.

Figure 2: *Qualitative diagrams of wave transmission through an infinitesimal shear layer between two media of relative motion. Grazing angle convention is used. Figures adapted from [35].*

layer of negligible thickness), the incident ray is refracted by an angle, dependent on the flow velocity difference (see Figure 2). Analogously to Snell's law in geometrical optics, the angle of refraction is derived by imposing the continuity constraint that the cross-sectional distance between the wavefronts along the interface has to be single-valued, irrespective of the region [35, pp. 708–710]. The rays bend towards the boundary when transmitted to the faster medium and away from the boundary when the velocity difference between the media is negative. As shown in the figure, a total reflection can occur at small grazing angles when the relative difference between the flow velocities is positive, while for negative flow velocity difference, a shadow zone exists, where refraction is not possible geometrically.

Part of the sound energy is transmitted at the interface between the two flows; however, some is reflected back. The incident wave encounters the change in impedance at the boundary. This change depends on the angle of incidence, the difference in the background velocity, the density of the media, and the speed of sound if the media are different. The reflection and transmission coefficients can be calculated based on these parameters [38], [35, pp. 710–712]. Due to the reflection at the shear layer, acoustic waveguides can form in a region of slower flow, surrounded by faster flow regions. These atmospheric 'ducts' can concentrate and direct the sound propagation (especially if the geometry and conditions lead to total reflections). Conversely, the sound emitted by a high-speed jet is refracted away at the boundary [35, pp. 713–714].

The shear layers have a certain finite thickness in practice, and the change in background flow conditions is gradual. Therefore, more complex models of sound transmission and reflection through finite shear layers have been investigated [38]. Furthermore, strong refraction and reflection effects are mainly present in high-speed flows since the effects depend on the Mach number. Finally, the ray-based approximation is limited to high-enough frequencies. Therefore, the concepts presented above serve as an approximation for incident wave behaviour, which only provides some theoretical intuition to the sound propagation in the background flow.

2.2.2 Atmospheric effects on sound propagation

As a practical example, under typical weather conditions, wind speed in the atmosphere varies with the height above the ground (the features on the ground, such as uneven topology, buildings and vegetation, slow the wind closest to the ground down while the top layers of the atmosphere are in a freestream flow). The gradual change in wind speed curves the sound waves away from straight propagation paths. By imagining a stack of infinitesimal layers of wind of increasing velocity, it is possible to apply the concept of refraction, depicted in Figure 2. For the sound propagating to the same general direction as the wind, but slightly upwards, each higher layer has a positive relative wind velocity and thus refracts the waves towards the horizontal, like in Figure 2a. After the critical angle is reached and the propagation is steered downwards, each interface between the layers has negative relative velocity and acts according to the Figure 2b, refracting the waves further down. Therefore, waves, which propagate downwind in the atmosphere, are bent down towards the ground. In contrast, sound, which propagates in the upwind direction, is bent upwards.

In general, the waves refract towards the lower effective speed of sound, which can also be affected by the temperature gradients. Typically, temperature decreases with height above ground, thus reducing the speed of sound as well, but under certain meteorological conditions, the temperature inversion may happen. However, the wind effects tend to dominate the sound propagation path [39].

The combination of atmospheric effects can cause various acoustic effects, such as shadow zones and focus regions (caustics) [34, Ch. 28]. Empirical models can be used to determine the speed of sound profiles in the atmosphere [4], [39]. Long-distance sound propagation can be modelled [40], [41] and measured [42]. However, the stratification of the atmosphere is very gradual. Therefore, the effects on sound are generally noticeable in long-distance propagation of the order of kilometres [5].

2.2.3 Sound in turbulent flow

Another background flow feature that affects the sound is turbulence. Turbulent eddies have sound scattering properties. The random nature of the eddies results in sound pressure fluctuations. For example, a line-of-sight measurement of noise from an aircraft a few kilometres away can have the standard deviation of sound pressure level up to 6 dB [34, p. 323]. For a directional sound source, turbulent scattering may cause attenuation at the receiver point since some sound deviates away from its initial direction [3]. Turbulent boundary layers may also absorb sound energy in the internal flow [43]. On the other hand, acoustic contrast between the shadow zones and the focus points due to atmospheric refraction or solid barriers diminishes due to turbulent scattering [39]. However, for spherically propagating waves, the attenuation due to turbulence may be negligible. The direction of scattering is random, so on average, the effect is counterbalanced by the scattering to all directions [34, p. 323].

2.2.4 Equations of motion for acoustic waves in non-uniform fluid

Previous examples of sound behaviour in background flow provide some intuition for aeroacoustics problems. However, to fully account for the interaction of acoustic waves and non-uniform flow around the human head, a more complex description of the waves has to be used. Theoretically, NS equations of fluid motion fully describe the fluid behaviour, so their time-domain solution would also incorporate acoustic pressure waves. However, in practice, this is an unfeasible option for simulating and predicting the wave behaviour due to computational limitations, so the system is typically decoupled into the background flow and the acoustic perturbations [44, p. 443]. The process is similar to the one presented for deriving RANS equations. Dependent variables, decomposed into the time-independent part and a time-dependent perturbation (e.g. $\mathbf{u} = \mathbf{u}_0(x) + \tilde{\mathbf{u}}(x,t)$), can be substituted to the conservation of mass (3) and momentum (1) equations. By rearranging and eliminating vanishing non-linear terms, a set of linearised Navier-Stokes (LNS) equations are derived:

$$\frac{\partial \tilde{\rho}}{\partial t} + \boldsymbol{\nabla} \cdot (\rho_0 \tilde{\mathbf{u}} + \tilde{\rho} \mathbf{u}_0) = \mathbf{M} \tag{11}$$

$$\rho_0\left(\frac{\partial\tilde{\mathbf{u}}}{\partial t}+(\tilde{\mathbf{u}}\cdot\boldsymbol{\nabla})\mathbf{u}_0+(\mathbf{u}_0\cdot\boldsymbol{\nabla})\tilde{\mathbf{u}}\right)+\tilde{\rho}(\mathbf{u}_0\cdot\boldsymbol{\nabla})\mathbf{u}_0= \\ -\boldsymbol{\nabla}\tilde{p}+\boldsymbol{\nabla}\cdot\left(\mu\Big(\boldsymbol{\nabla}\tilde{\mathbf{u}}+(\boldsymbol{\nabla}\tilde{\mathbf{u}})^{\top}\Big)+\left(\mu_{\mathrm{B}}-\frac{2}{3}\mu\right)(\boldsymbol{\nabla}\cdot\tilde{\mathbf{u}})\mathbf{I}\right)-\mathbf{u}_0\mathbf{M}. \tag{12}$$

Compared to the incompressible RANS equations, the LNS equations retain the compressibility assumption. Furthermore, a mass source term $\mathbf{M}$ is added here to describe the sound sources in the domain. Finally, bulk viscosity μ_{B}, disregarded in the previous NS formulation, is reintroduced here due to its effect on the attenuation of sound waves [45]. These equations set an adiabatic formulation (i.e. without heat exchange) of the perturbed fluid behaviour. For a more accurate representation, the energy (heat) conservation equation has to be included. Furthermore, a linearised thermodynamic equation of state links the density perturbation to pressure and temperature variations through the coefficients of isobaric thermal expansion and isothermal compressibility (the complete set of equations is given in [44, pp. 443–448]).

The presented equations were derived without explicitly accounting for the turbulent fluctuations. A triple variable decomposition can be used to separate the mean flow variables (e.g. $\mathbf{u}_0(x)$), the harmonic motion ($\tilde{\mathbf{u}}(x,t)$), and the turbulent motion ($\mathbf{u}'(x,t)$), as presented in [46]. Then, using the time and phase averages to eliminate each component, the set of LNS equations can be derived. They contain an additional oscillating Reynolds stress tensor term, which can be represented by the turbulent viscosity, discussed previously. Therefore, the effect of turbulence in Equation 12 is accounted for by using the effective viscosity, which is the sum of dynamic viscosity (property of the material) and turbulent viscosity (obtained from the background flow simulation).

Conceptually, the terms in Equation 11 and Equation 12, which have a convective operator applied to the oscillating flow (e.g.$(\mathbf{u}_0\cdot\boldsymbol{\nabla})\tilde{\mathbf{u}}$) describe how the oscillations are transported along the direction of background flow. The diffusive terms, which are represented by the Laplacian and include viscosity coefficients, determine how the perturbations spread. Source terms supply the energy to the system. Finally, reactive terms, expressed as gradients of the background flow, represent the effect of the oscillations on the mean flow; however, these terms might lead to the growth of instabilities in the simulations and may need to be removed from the equations in some situations [44, pp. 447–448].

The LNS equations can be solved in the frequency domain by assuming a harmonic time-dependent perturbation of a form $e^{-i\omega t}$. The time derivatives are thus replaced by a factor $-i\omega$. The frequency-domain solution simplifies the boundary conditions and the result analysis [46]. A *slip* boundary condition is typically used for the acoustic wave propagation, which imposes zero perturbed flow normal to the boundary (i.e. $\mathbf{n}\cdot\tilde{\mathbf{u}}(\partial\Omega)=0$).

The equations that govern the fluids and their waves are intricate, and their effect on wave behaviour is hard to see intuitively. However, computer simulations provide a powerful tool to visualise and analyse the implications of the theoretical model.

2.3 Characteristics of the human voice

The sound source of interest for the study of sound propagation around the human head is the human voice. Aside from ingressive speech, produced by inhaling the air [47], most of the human speech sounds are made in conjunction with the exhalation of air from the lungs, via trachea, larynx, pharynx, the oral and nasal cavities, to the outside [48, p. 6]. The sound is produced by modulating this outward flow. To produce the voiced speech sounds, such as vowels and voiced consonants (e.g. /n/ or /z/), the vocal folds, which are situated in the larynx, are set into a quasi-periodic motion, repeatedly opening and closing the glottis (an orifice between the vocal folds) at an auditory rate [49, p. 80]. In the case of unvoiced phonemes (e.g. consonants like /p/ or /s/), the vocal folds do not vibrate, and the sound instead arises from a forced stream of air through constricted openings and sharp edges of the vocal tract [48, Ch. 2]. Articulation of different phonemes happens by varying the shape of the vocal tract (especially the oral cavity), which acts as an acoustic filter.

2.3.1 Frequency content of speech

The characteristics of the vocal folds, such as their mass and stiffness, determine the fundamental frequency of the voiced speech. An average fundamental frequency of the conversational speech is around 120 Hz for males and 200 Hz for females [49, Sec. 5.1.2]. The fundamental frequency is varied by the speaker to help express a specific mood of speech or, in the case of tone languages (e.g. Mandarin Chinese), convey a lexical meaning. The pitch variation is much higher in the singing voice and can reach up to 1500 Hz in the soprano range [49, Sec. 5.1.2].

The shape of the vocal tract, which depends on the placement of the teeth, the lips, the tongue and the palate, changes the resonances of the tract, known as the formants. The relative position of the formants in the frequency spectrum is one of the key characteristics that define differences between the phonemes. Generally, for vowels, the frequency of the first and the second formant (which are the most important for the vowel quality) can be in the range from approximately 250 Hz to 1000 Hz and from 600 Hz to 2500 Hz, respectively [50]. The most critical frequency range for speech communication (discovered through the research on early telephone communication and known as the *telephone band*) is from 300 Hz to 3400 Hz [49, p. 336]. Within this range, the sound energy peaks around 500 Hz in casual speech and around 1250 Hz in shouted speech [51].

2.3.2 Directivity of the voice

The speech, produced in the vocal tract, is radiated outwards mainly through the mouth and the nose. Additionally, some radiation happens through the neck as well as the chest (especially in a singing voice) [48, p. 7].

The directivity measurements of the singing voice [52] and speech [53] show frequency-dependent directivity patterns. In the lowest frequency bands, the size of the head is smaller than the wavelength, so the voice is almost omnidirectional: the radiation to the back of the head is attenuated by a few decibels as compared to the

front. For frequencies above 1 kHz, the wavelength is comparable or smaller than the dimensions of the head, so the voice becomes directional, and most of the energy is radiated directly outwards from the mouth. For example, at 4 kHz, the difference between the radiation to the front and the back of the head is around 10–20 dB.

The directivity of the voice was also found to be affected by the wind gradients around the head [14]. For the voice emitted downstream, the wake region appears to create an acoustic waveguide and focus the sound energy downwind (cf. 'atmospheric duct' discussed in Sec. 2.2.1).

2.4 Human hearing mechanism

All surrounding sounds (including one's own voice) are registered by the human hearing mechanism, which comprises the outer, the middle and the inner ear. Most external airborne sounds arrive at the pinna and are directed through the ear canal to the eardrum, which forms the boundary between the outer and the middle ear. The ossicles of the middle ear match the impedance between the eardrum and the inner ear. Finally, the sound is converted to neural signals in the inner ear and is transmitted to the brain, where it is processed.

Humans are able to identify acoustic pressure variations as low as 20 µPa (0 dB SPL, hearing threshold) and as high as 60 Pa (130 dB, approximate threshold of pain) [49, p. 154]. The audible frequency range is approximately 20 Hz to 20 000 Hz. The human perception of loudness is a complex phenomenon and depends on the frequency range of the sound and its absolute level, but a 1 dB difference in SPL of a sound event is generally considered to be a just-noticeable difference of loudness for a wide range of SPLs [49, Sec. 10.2].

Some acoustic sound and mechanical vibration can propagate via the bones of the skull and agitate the middle and inner ear directly. This contribution is typically negligible for external airborne vibrations because its energy is 30 to 60 dB lower than from the sound, arriving via the outer ear [54]. However, bone conduction provides a significant contribution when listening to one's own voice. The lack of the bone-conducted part of the voice is the main reason the recorded voice often sounds strange to its author. The relationship between the bone and the air conducted parts of one's own voice was measured for different phonemes [55]. It was shown that the two contributions were of equal importance but depended on the frequencies and the types of phonemes used. For example, for nasals (e.g. /n/), the bone-conducted contribution was 12 dB higher than the air-conducted part in 1–2 kHz, whereas plosives (e.g. /p/) had a generally lower bone-conducted contribution than the air-conducted one and the bone-conduction for them peaked in the frequencies below 300 Hz. The bone-conducted part mostly dominated the perception of vowels between 1 kHz and 2 kHz (depending on the vowel type) but was equal to or weaker than the air-conducted part in lower and higher frequency ranges.

Generally, the bone-conducted and the air-conducted parts contribute to the self-audition at different levels depending on the frequency. Therefore, affecting one of the contributions may affect the overall balance of the sound and change the perception of one's own voice.

3 Modelling methodology

The wind effect on the sound, propagating from the human mouth to the ears, can be examined by modelling the physics of this system. Partial differential equations presented in the previous chapter, which govern the fluid motion and sound wave behaviour, are essential in the simulation process. However, it is impossible to find their exact analytic solution for most real-life situations. Numerical methods are thus used to model the system's behaviour: the continuous nature of the functions, their derivatives, and integrals are adapted to the numerical computational domain by replacing them with discrete approximations.

This chapter briefly describes the numerical method used in this thesis to simulate the sound propagation from the mouth to the ears in background wind, known as the finite element method (FEM). It then discusses practical considerations taken when setting up the CFD and the acoustics models in COMSOL Multiphysics® 5.5 modelling software.

3.1 Overview of the finite element method

The full theory of the FEM and its implementation in software is beyond the scope of this thesis and can be found in dedicated textbooks (e.g. [56], [57]). While creating the models in COMSOL does not require in-depth knowledge of the underlying numerical schemes, this section presents the method's basic principles so that the results could be better understood.

The finite element method replaces continuous dependent variables (such as velocity and pressure fields or turbulent kinetic energy) by their piecewise approximations, commonly constructed from a set of polynomial basis functions [57, Ch. 1]. Different polynomial order can be used, which results in an increasingly more accurate representation of the real functions at the expense of a higher number of degrees of freedom required to construct the higher-order polynomials. The models created for this thesis used a linear discretisation; therefore, the discussion is also limited to linear basis functions.

As an example, a dependent variable u can be approximated by $u \approx u_\mathrm{h}$, such that:

$$u_\mathrm{h} = \sum_i u_i \psi_i, \tag{13}$$

where ψ_i represents linear basis functions and u_i denotes the coefficients, associated with them. The spatial modelling domain is typically discretised to a mesh of nodes. Then the basis function ψ_i is defined as equal to one at the node i and zero at all other nodes. Figure 3 shows an example of such discretisation in a one-dimensional domain. The tent functions, presented in the figure, form a set of basis functions. Their respective coefficients are found by evaluating the continuous function at their respective node points. As presented in the example, the chosen discretisation nodes need not be uniformly distributed; instead, the areas where large gradients of the variable are expected could be meshed denser to better approximate more rapid variations.

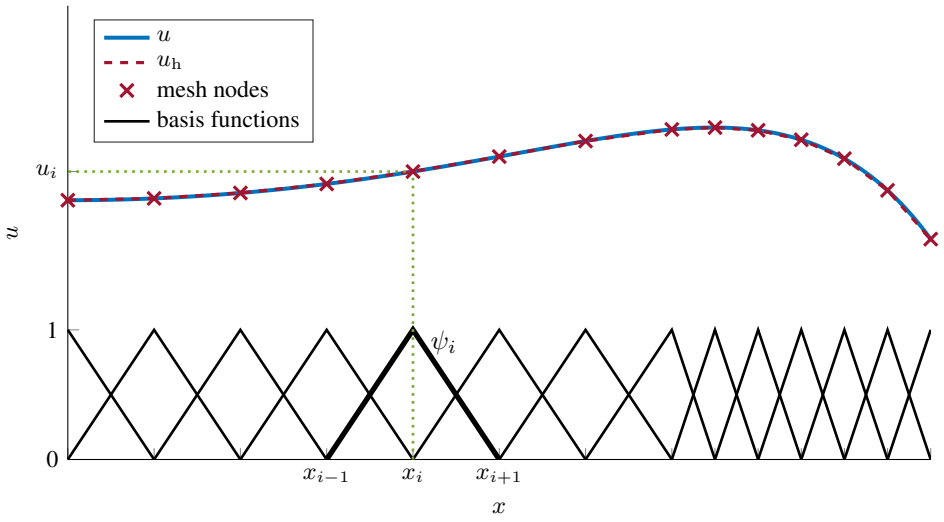

Figure 3: *Example of FEM discretisation with linear basis functions in 1D. The basis function ψ_i is equal to one at mesh node x_i and zero at all other nodes. The coefficient u_i for ψ_i is the value of the continuous function u at x_i. u is approximated by piecewise u_h, which is a sum of $u_i\psi_i$. Figure adapted from [58].*

The next step in FEM formulation is to convert the PDEs representing the system from the strong form (as presented in the previous chapter) to their weak integral form. The weak formulation approximates the absolute continuous validity of the function. Instead, the equations hold over a set of test functions. Each test function is defined to sample a small domain range (the same basis functions are used in this case). The weak form is found by multiplying the equations in their strong form by the test functions and integrating them over the domain [58]. Then, the order of derivatives is reduced using integration by parts (or divergence theorem in higher dimensions). The weak formulation improves the stability of the numerical model since some derivatives, especially at the boundary, are hard to evaluate numerically due to the discontinuities of the functions [59]. Although the final weak form of the equations at each node uses integration over the whole domain, the integrands contain products of the test functions and the sum of the basis functions from Equation 13. The two functions overlap and are non-zero only in a small area of the surrounding nodes (as can be seen by the overlap of the neighbouring basis functions in Figure 3). Thus, the integration is evaluated only over the surrounding set of points [58]. For the nodes that appear on the boundary, the equations must also include the boundary conditions (such as the no-slip condition, discussed in Sec. 2.1.4). The final set of equations is assembled into a system (a.k.a. 'stiffness') matrix. The diagonal elements of the matrix correspond to the contributions from the fully overlapping basis function, and other non-zero elements arise from the partially overlapping basis functions at the neighbouring nodes; otherwise, the matrix is sparse. Finally, the system of equations can be solved directly by inverting the system matrix, but current solvers employ more efficient matrix equation solving techniques.

The method, briefly described above, is used for stationary, time-independent

simulation. This type of study was used to model the background fluid flow. In the case of the acoustics simulation, two types of models were created: frequency-domain and time-domain. For the time-domain study, an additional time-stepping method is implemented. It discretises the time derivatives (for example, to finite differences) and uses time-stepping to solve the system of equations at each time instance [58].

The theory of the FEM, presented in this section, provides a simplified overview of the numerical method used to model the physics of a system. Commercial software, such as COMSOL, includes many additional techniques and improvements for better computational accuracy, stability, and efficiency.

3.2 Meshing

The previous section used a 1D domain as a simplified example to explain discretisation. The 2D modelling domain used in this thesis requires different mesh elements, namely triangular or rectangular shapes, which also influence the shape of the basis functions. Generally, the mesh quality dramatically affects the model stability, the convergence and validity of the results and the efficiency of the calculation. Fundamentally, the mesh has to cover the whole domain without creating voids or overlaps [60]. Further concerns are the overall quality (skewness) of each element and the balance between a sufficient resolution and computational speed. Generally, triangular (or tetrahedral in 3D) mesh elements can mesh a wide range of geometries while also keeping their skewness low. Therefore, they form a basis of the mesh for most of the physics models in COMSOL [61]. However, some specific refinements are needed, depending on the physics used, and they are detailed below.

3.2.1 CFD mesh

In the fluid flow simulation, the highest flow velocity and pressure gradients occur around no-slip boundaries and shear layers. Therefore, the mesh resolution has to be refined around boundary surfaces to improve the representation of rapidly changing variables.

The boundary layer flow is anisotropic: the velocity gradient is steep along the direction perpendicular to the boundary. For this reason, a structured set of anisotropic rectangular elements are used to mesh the first few mesh layers around the solid surfaces, creating an onion-like layer structure around the boundary. These elements are broader in the direction parallel to the surface and shorter perpendicularly from the surfaces. By gradually increasing their overall size, the mesh density can transition from fine line elements on the boundary to coarser unstructured triangular mesh away from the boundary layer.

Generally, the COMSOL meshing process is highly automated and aims to create the best possible mesh for a given geometry and physics used. The primary CFD mesh features used in this work are very fine line elements on the no-slip boundaries of the models, six structured boundary layers around them with a stretching factor of 1.2, and a free triangular mesh for the rest of the domain. The created mesh is denser around the cross-section of the head, where the gradients are the highest, and

coarser away from it, reducing the computation time.

3.2.2 Acoustics mesh

In the acoustic wave simulation, the mesh size must be small enough to resolve the desired wavelengths. Therefore, the mesh density depends on the minimum wavelength (the maximum frequency) modelled. A common rule of thumb for the mesh is at least ten elements per wavelength for the first-order (linear) mesh elements [62]. Furthermore, the acoustics simulations require a relatively uniform mesh. These considerations were taken into account when creating the mesh for the acoustics simulation in COMSOL.

Additional meshing requirements are present in the frequency-domain simulation. The models created for this thesis aim to simulate a free-field domain; however, modelled geometries are of finite size (the smaller they are, the easier it is for the computations). In the time-domain simulation, the free-field condition is achieved by windowing the simulated acoustic wave before the reflections from the outer boundary travel back to the receiver. In the frequency-domain model, a fully absorptive outer boundary has to be used to imitate the infinite domain. A Perfectly Matched Layer (PML) serves this purpose. PML is an artificial domain, which uses a complex coordinate stretching to absorb the incident waves [63, p. 387]. It is drawn as an additional domain, which surrounds the exterior of the physical domain. The exact dimensions used for a specific geometry are not critical because COMSOL applies the stretching automatically, depending on the wavelength of the acoustic wave. The optimal meshing for this layer in 2D is a structured rectangular mesh of around eight elements in the outward direction of wave propagation [44, p. 186]. Other PML parameters chosen are based on the geometry used and information in COMSOL tutorials [64].

3.2.3 Multiphysics mesh mapping

Coupling between two different physics simulations is required to model the sound interaction with the fluid flow. As discussed above, the optimal mesh requirements for CFD and the acoustics simulation differ. Therefore, the background flow parameters computed in a CFD simulation have to be mapped to the acoustics mesh before running the acoustics simulation. A dedicated ‘Background Fluid Flow Coupling’ interface and ‘Mapping’ study handles this mapping in COMSOL.

3.3 Model geometry and setup

Several modelling iterations and refinements were undertaken to simulate the sound-flow interaction. The models were limited to a two-dimensional domain. Although attempts were made to model a whole three-dimensional geometry, a lack of meshing expertise and software resources hindered the success (solvers did not converge when solving the CFD models). The use of the ‘Puhti’ supercomputer at CSC was investigated; however, batch simulations on the cluster proved to be slower due to the high workload of the server and limited parallelisation abilities of the COMSOL

computation process. Nonetheless, two-dimensional simulations exhibited distinct characteristics, which can be extrapolated to 3D geometry. This section presents the geometrical setup for the two final 2D simulations used in this thesis.

The differences between the two simulations presented here lie in the geometry of the model 'head' and the domain of the acoustics solver (time versus frequency). Both geometries are shown in Figure 4 and Figure 5. The model, presented in Figure 4, simplifies the horizontal cross-section of the head to a circle of 0.1 m radius. The fluid domain is bounded within a circle of 1.5 m radius. This geometry was used for the frequency-domain study, so the outer layer of width 0.2 m was dedicated to PML in the acoustics simulation. Figure 5b presents the second model, which uses a cross-section of a three-dimensional head model, shown in Figure 5a. An approximate length of the semi-major axis of the head cross-section is 10 cm, and the semi-minor axis is 8 cm. The outer domain boundary is at 1 m radius from the centre. This geometry was used for the time-domain acoustics study. Compared to the circular model, the cross-section of the head has finer features, especially around the ears; therefore, its mesh had to be finer around those areas compared to the mesh of the circular model.

For each of the models, the simulation was divided into three steps. Firstly, the turbulent flow was computed for a chosen wind speed and direction using a CFD model mesh. Then the background flow parameters were mapped from the CFD solution to the acoustics mesh. Finally, the acoustics simulation was run using the acoustics mesh with background flow parameters. A parametric sweep interface ran

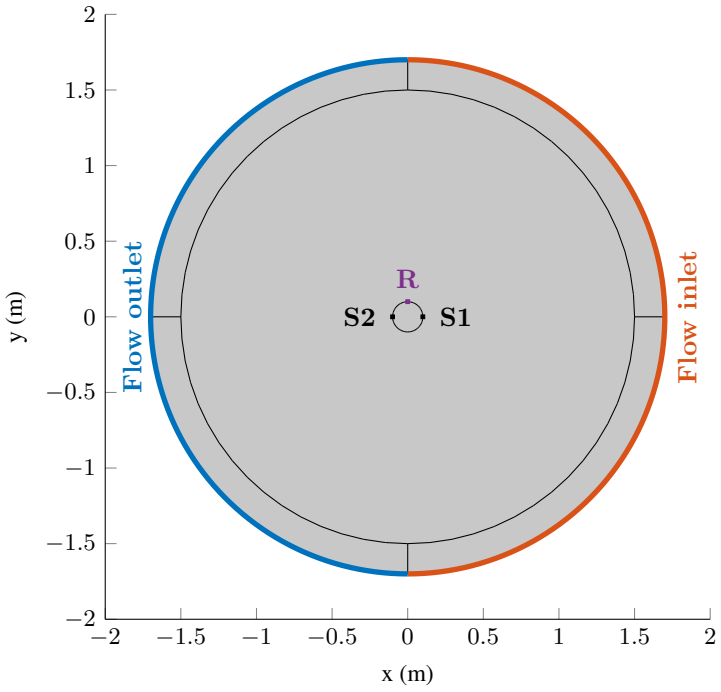

Figure 4: *Geometry of the 2D frequency-domain simulation. S1 is the source position in the upwind and S2 in the downwind scenario. R is the receiver position. In the acoustics simulation, the outermost layers of the circular domain are defined as PML.*

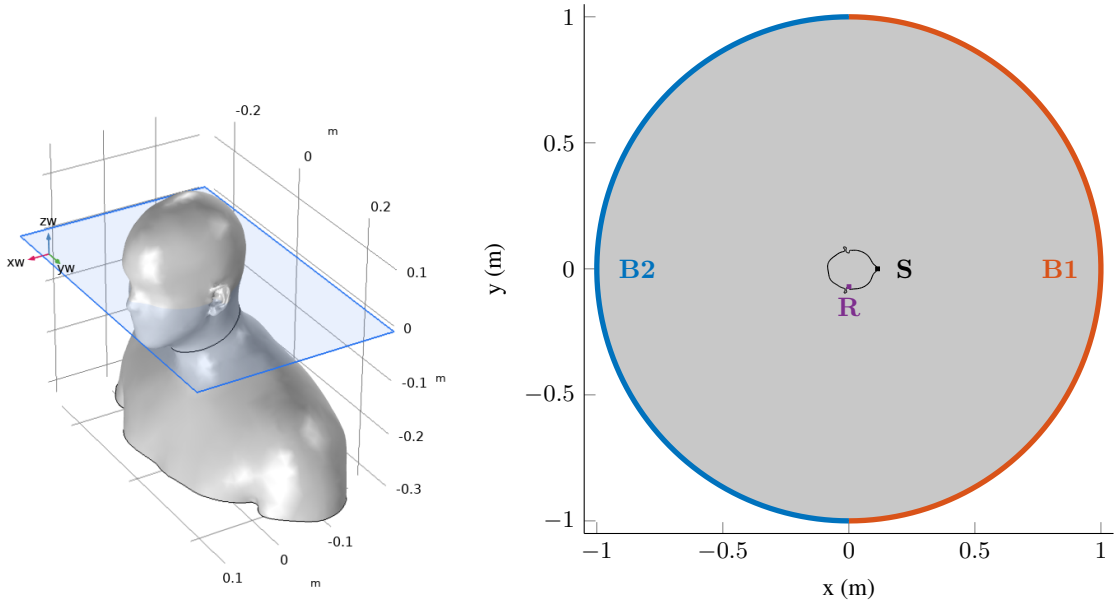

(a) *3D head and torso model with a cross-section plane, used for the 2D model. The 3D model is taken from [65].*

(b) *The 2D model geometry. B1 is the flow inlet, and B2 is the flow outlet in the upwind scenario (vice versa in the downwind case). S is the source (mouth) position, R is the receiver position (right ear canal).*

Figure 5: *Geometry of the 2D time-domain simulation with a cross-section of the model head.*

the model with different combinations of wind speeds and directions. The sections below present more detailed information on both model setups.

3.3.1 CFD model setup

The SST turbulent flow physics interface was used to model the fluid flow in COMSOL. The flow was modelled as incompressible, and the standard properties of air at 1 atm pressure and 20 °C were used in the simulation.

No-slip boundary conditions were assigned to the cross-sections of the head. The outer circular boundaries were split in half: one semicircle served as an inlet, the other as an outlet. The inlet was assigned with a velocity boundary condition, where the velocity of incoming air was defined to be parallel to the x-axis. A set of velocities from 6 m/s to 24 m/s as well as 0 m/s (stationary case) were used. The outlet acted as a zero-relative-pressure boundary condition. The circular head model is symmetric, so the inlet and outlet positions were fixed, and different wind directions were modelled by changing the position of the source in the acoustics simulation (as shown in Figure 4). However, the inlet and the outlet of the asymmetrical second model were swapped for the upwind and the downwind scenario (i.e. in Figure 5b, B1 boundary acted as an inlet in the upwind condition and as an outlet in the downwind condition. The opposite was the case for the B2 boundary).

A stationary solver with wall-distance initialisation (required for the turbulence model) was used to compute the velocity, pressure, and turbulent viscosity fields. These variables were then mapped to the acoustics mesh and used as background parameters in the acoustics study.

3.3.2 Acoustics model setup

A linearised Navier-Stokes interface was used to simulate the acoustic wave propagation around the cross-section of the head in COMSOL. All the boundaries of the model were adiabatic, except in the case of PML.

The sound, radiating from the mouth, was modelled as a domain mass source. A Gaussian distribution described the location and the size of the source. Its peak was defined at a boundary point (letter S in Figure 5b for both wind directions, S1 in Figure 4 for the upwind case and S2 for the downwind scenario). The spatial source spread (standard deviation) in both models was 1 cm. In the time-domain simulation, the Gaussian source was also time-dependent, with 0.1 ms standard deviation and the peak at 0.5 ms. This 5 σ shift of the peak avoided sudden gradients at the beginning of the model, reducing the probability of model instabilities.

A domain probe in COMSOL recorded the data at the position of the ear (letter R in the figures). The position of the source was also used for comparison. The simulations modelled the frequencies up to 8000 Hz. The frequency-domain simulation modelled 83 frequencies in a logarithmic scale from 100 Hz. Lower frequencies were not modelled because of the domain size constraints (the minimum distance from the source to the physical domain boundary is 1.4 m, which corresponds to $343/1.4 = 245$ (Hz); the complete wavelength of sound could only be resolved for the frequencies above this limit). The specific frequencies modelled correspond to the frequencies used in the measurements, described in Chapter 4. In the time-domain simulation, the data was recorded at 96 kHz sample rate; however, the time-stepping of the actual simulation was denser and set automatically by COMSOL. The total simulation time was around 4.6 ms, which is the maximum time before the sound is reflected from the outer boundaries and propagated back to the position of the ears.

The exact solver configurations used in the time-dependent and frequency-dependent studies were set automatically by COMSOL. COMSOL Acoustics Module User's Guide [44] and COMSOL support were consulted to achieve the best stability and performance of the models. The results obtained from the simulations were analysed and plotted in MATLAB.

4 Measurement methodology

A physical experiment was also devised to test the possible effect of wind around a human head on the sound propagation from the mouth to the ears. A simplified arrangement was used with an artificial speaker and microphones placed around a model body, imitating the mouth and ears, respectively, and the sound recorded in a set of different wind speeds and directions. The measurement had a double function as a validation tool for the computer simulations, which imposed certain geometrical limitations on the setup. This chapter outlines the setup of the conducted experiment, its procedure and data analysis used to obtain the final results.

4.1 Discussion on measurement setup

The physical experiment aimed to create a controlled environment and a reproducible procedure, with unaccounted factors minimised. For sound measurements in the wind, three main challenges were identified: finding a stable wind source, designing a simplified yet representative geometry, and minimising undesired acoustic effects (such as sound reflections from external surfaces and the effect of background noise). The following paragraphs discuss the considerations taken to address these challenges.

Firstly, a relatively uniform and wide wind velocity field had to be found to represent a free-field condition within the measurement window. Various wind generation methods for testing wind noise in microphones have been reported in the literature, such as radial and axial fans, wind tunnels, rotating booms in anechoic chambers, car drives, and measurements in real wind [66]. The methods differ by their ability to produce stable and uniform flow, background noise produced by the generator, and accessibility. Wind tunnels, for example, suffer from high background noise, early acoustic reflections due to their limited size and restricted accessibility. Due to the challenges of indoor wind generation, measurement methodology, proposed in [14], was adapted for this experiment: a vehicle with the measurement rig on the roof was driven at a constant speed in a free field. Due to the relativity of motion, the movement of the source replicated the wind blowing in the opposite direction. Although it was difficult to control the exact wind speed and direction in the open air, anemometers monitored and recorded the wind speed while a visual wind vane informed about the wind direction during the experiment. The measurement segments were then sifted in the post-processing stage based on the stability of the wind to minimise the effect of wind variation on the final results.

Secondly, the two-dimensional domain used for the simulations influenced the shape of the measurement rig. A long cylinder of a diameter, comparable to the human head, was used, imitating the flow around a cross-section of the human head. Consequently, the discussion of wind effects was limited to horizontal flows and symmetric circular head geometry. The turbulent flow and sound propagation from point sources behave differently in the 2D model compared to the physical 3D world (point source in 2D corresponds to a line source of infinite length in 3D). However, the study was mainly interested in relative differences between the responses for different wind conditions, while the discrepancies in turbulent effects were considered minor

compared to the main effect from boundary layer flow gradients. Although a 2D simulation of a circle corresponds to a cylinder of infinite length, the measurement rig was limited to 1.5 m height due to technical constraints. The top of a finite cylinder generally affects the form and the size of the turbulent wake region behind the cylinder [67]. Therefore, the speaker was installed mid-height (0.75 m) to minimise any potential effects from the cylinder top and the roof of the van.

Finally, the influence from background noise due to wind and the car's engine had to be minimised. The use of high sensitivity compression driver ensured a high SNR in a noisy environment. Furthermore, omnidirectional pressure microphones were used due to their lower sensitivity to wind noise (the airtight volume behind their membranes ensure lower membrane compliance, as compared to directional pressure gradient microphones [68]). Additionally, microphone windshields reduced the wind-induced noise on the microphone. Generally, the airflow might be slowed down, and the turbulence effects increased within and around the windshields due to the change in local surface roughness. However, this influence on the measurements was deemed minor: the main wind effect on sound was assumed to develop along the sound propagation path from the speaker to the microphone, whereas the windshields affected the airflow primarily at the microphone position and behind it. Furthermore, only relative sound level differences were studied, so any potential biases, which affected all the measurements equally, were eliminated in the analysis stage.

SNR was further increased by choosing an appropriate input signal to be played through the speaker. Typical IR measurements may use exponential sweep or noise burst techniques. Although the exponential sine sweep technique with an inverse filter provides a good SNR, the method is only valid for a time-invariant system [69]. Due to the highly unsteady flow, the sound propagation in the wind cannot be assumed to be time-invariant. On the other hand, white or pink noise has a spectral profile, which is hard to distinguish from the background noise. For these reasons, a multitone signal was chosen for the measurements instead. The signal is typically used for fast distortion and transfer function measurements [70]. It is formed from a series of sine waves at different frequencies. A logarithmic order of frequencies can be chosen to avoid the periodicity of the signal and reproduce a spectral density in line with octave-band audio formalism. The measured frequency response at the multitone frequencies can be assumed to be a representative sample of the actual broadband response if the density of the tones is high enough. The length of the FFT window is typically chosen prior to generating the multitone signal, and the frequencies of the tones are set to match the desired FFT frequency bins. This way, spectral leakage to other frequency bins is avoided at the analysis stage without additional windowing. To achieve the highest possible dynamic range and SNR, a crest factor (CF, defined as the ratio between the signal peak and RMS values) of the signal has to be minimised [71]. CF is affected by the phase relationships between the tones, and techniques exist to find its lower bound [72]. For simplicity, the multitone signal used in this experiment had the phases of the tones randomised while imposing a condition of maximum CF allowed.

The considerations of the measurement setup presented above informed the final measurement design and procedure, presented in the next section.

4.2 Measurement equipment

Table 1 reports the equipment used for the measurements. The measurement rig was built using a 20-centimetre-diameter 1.5-metre-length PVC pipe. A 3.5 cm hole was cut in the middle of the pipe for the driver. The driver was fit inside the pipe using 3D-printed spacers (the depth to the driver was 5 cm). The inside of the pipe was filled with absorptive foam material to eliminate resonances of the enclosure. The microphones were fit on the outside of the cylinder at the same height as the speaker (0.75 m) 90° away from the 'mouth' to represent ear positions. A control microphone was also placed below the driver to monitor the sound at the position of the 'mouth'.

The measurement rig was secured on the roof by wire ropes on either side of the roof bars, as seen in Figure 6. Different wind directions to the speaker were imitated by rotating the cylinder. The measured directions were 0° (upwind condition, shown in the pictures), 180° (downwind condition) and 90° (sideways condition, not discussed in this thesis). Two anemometers were installed on the roof: one used to monitor the wind speed live while driving, another one recorded via the audio interface. The wind vane was also installed, and its position recorded using GoPro, attached to the front windscreen (Figure 6a).

The multitone signal, played through the speaker, was composed of a hundred logarithmically-spaced sine tones of randomised phases within the frequency range of 50 Hz to 10 000 Hz. An FFT window of 2^{16} samples (which equates to approx. 1.365 s signal length for a 48 000 Hz sample rate used) was chosen, and the tone frequencies were matched to the corresponding FFT frequency bins. Five-second sound segments were used with 2.5-second silent gaps in between so that the background noise could

Table 1: *Summary of the equipment used in the measurements*

Item	Model	Notes
Driver	BMS 4594ND-MID	1.4″ two-way compression driver; only the mid-range driver was used.
Microphones	DPA 4061	Omnidirectional microphones; max peak SPL = 144 dB .
Windshields	Rycote Windjammers	Used on top of foam windscreens.
Amplifier	S.M.S.L. SA-50	50 W class D amplifier.
Audio interface	RME UFX+	
Recording software	Reaper DAW	
Cup anemometers	Inspeed Vortex	Cateye Velo8 cyclocomputer used to monitor wind speed. Data recorded via audio interface.
Wind vane	Inspeed e-Vane	Direction inspected visually via GoPro cameras.

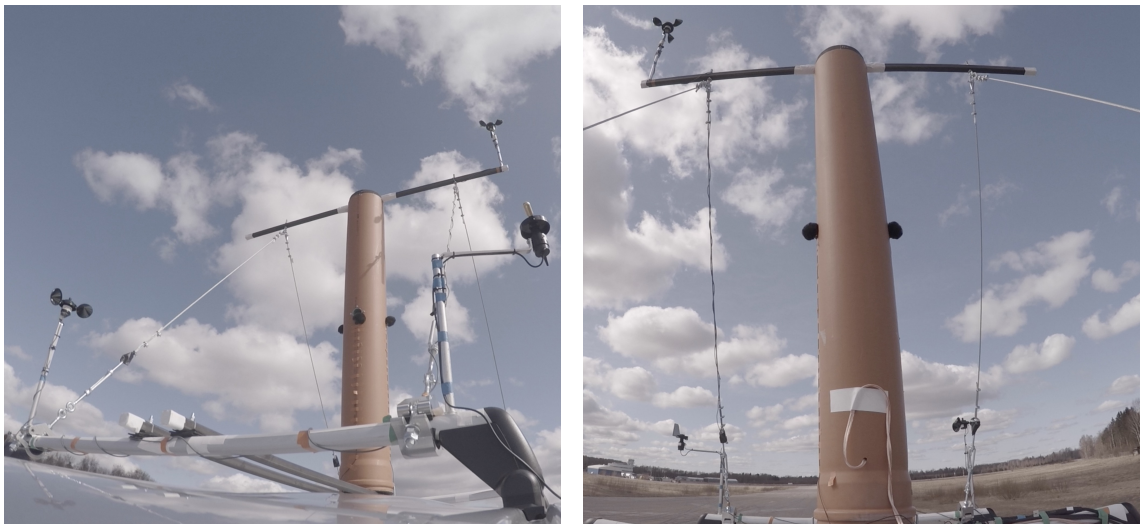

(a) *Front.* (b) *Back.*

Figure 6: *Still images from GoPro footage of 0° (upwind) measurement setup.*

be captured independently of the signal and SNR estimated.

4.3 Measurement conditions and procedure

The experiment was conducted in Helsinki-Malmi airport. A 500 m section of the runaway, which ran east-to-west, was used. The direction of the drive was kept constant throughout the measurements.

The sky on the day of the measurements was partly cloudy with some sunny spells. The temperature was 5 °C in the morning at the start of the measurements and increased to 12 °C in the afternoon. Relative humidity decreased from 70 % in the morning to 36 % in the afternoon. The ambient pressure rose from 102.0 kPa to 102.2 kPa.

Amplifier level and microphone gains in the audio interface were fixed throughout the measurement. The amplifier gain dial was set slightly over half the maximum to avoid distortions from the amplifier and the driver. The stability of the sound source throughout the measurements was verified by measuring SPL at the position of the side microphone with a calibrated Class 1 Sinus Tango sound level meter. 15-second-long measurements of the multitone signal were recorded after each rotation of the speaker while the car was stationary. For all three directional setups, the recorded A-weighted equivalent SPL was $L_{\mathrm{Aeq}} = 114\,\mathrm{dB}$. Measured background sound level was $L_{\mathrm{Aeq}} = 49\,\mathrm{dB}$.

For each source direction, measurements were conducted in 6 m/s, 12 m/s, 18 m/s, and 24 m/s wind speeds. Based on the live anemometer readings, the driving speed was adjusted to correct a mismatch between the wind speed and the driving speed due to ambient wind. Each drive for a specific wind direction and speed combination was repeated three times. Before and after every drive (i.e. on both sides of the runaway), a single five-second multitone burst, surrounded by silence, was recorded.

These stationary measurements were later used to calculate the difference between the frequency response, measured in the wind versus no-wind conditions. Every measurement conducted while driving was composed of a set of five-second multitone signals separated by silent gaps. The number of them differed depending on the drive speed, which limited the duration of each drive.

4.4 Data analysis

Data obtained from the measurements contained multiple repetitions of similar wind conditions, so the analysis step was needed to review the data, select the segments with the most stable wind measurements, find representative magnitude response for each condition, and plot the differences between them.

Wind measurement recordings helped to select the most stable measurement segments. Anemometer readings were recorded as a series of impulses, one for each rotation of the anemometer cups. The wind speed could be calculated by either measuring the length of the gaps between individual pulses or counting the number of pulses in a given period. The calibrated rotation 'distance' between each pulse, provided by the device manufacturer, was used in the calculation.

In order to select the most stable wind samples, each measurement was first scanned using `findpeaks` function in MATLAB to detect the impulses, and an instantaneous wind speed was calculated for each gap between the peaks. Next, a moving window of 2^{16} samples (corresponding to the multitone FFT size) selected non-overlapping measurement periods with the standard deviation of instantaneous speeds below 0.4 m/s. The stationary measurements were restricted by 2.5 m/s instantaneous wind speed limit instead. The instantaneous speed measurements were subject to more statistical noise; therefore, average wind speed over the entire length of each selected segment was used in further stages of the averaging process. A set of background noise segments of the same length, recorded just before or after each signal measurement, were also selected to represent the existing noise floor.

An FFT was then computed for each measurement segment. There were multiple segments chosen from each driving condition. Therefore, the mean magnitude response for each condition was calculated using incoherent averaging of the magnitude spectra to reduce noise variance [73, Sec. 11.3]. Incoherent averaging (over magnitudes) over a coherent one (over complex frequency spectra) was chosen because the signal phase alignment was affected by the wind fluctuations.

The same averaging process used for signal segments was also implemented for the background noise samples. The noise floor for each averaged measurement was then estimated using the peak `envelope` function in MATLAB. A 20 dB SNR criterion was imposed on all the multitone peaks: if the magnitude of the peak was lower than 20 dB above the noise floor at that frequency, the peak was discarded from further analysis.

The stationary measurements taken on both sides of the runaway were analysed and averaged using the same techniques as the measurements taken while driving. The mean magnitude response for each wind velocity was compared to its corresponding stationary response: the decibel levels of the measurements in the wind

were subtracted from those in no-wind conditions. Only the magnitudes of multitone frequencies, which mutually satisfied the SNR criteria, were used. The magnitude responses in the wind were compared to their corresponding no-wind responses measured around the same time (instead of using a single averaged zero-wind response) to minimise the biases of each measurement caused by the ambient weather and noise conditions. The obtained relative magnitude responses for each wind condition were ultimately compared against each other to establish the effect of wind on the recorded magnitude responses.

Uncertainty of the averaged magnitudes at each frequency was estimated by calculating the standard error of the mean (SEM). SEM is defined as the standard deviation divided by the square root of the number of measurements used in the averaging, i.e. (assuming the measurement and its associated FFT magnitude spectrum in units of acoustic pressure):

$$\sigma_{\bar{\tilde{p}}} = \frac{\sigma_{\tilde{p}}}{\sqrt{N}} \tag{14}$$

The error was converted to the decibel scale using standard error propagation methods [74]:

$$\sigma_{\overline{L}} = \frac{\partial \overline{L}}{\partial \bar{\tilde{p}}} \sigma_{\bar{\tilde{p}}} = \frac{\partial 20 \log_{10}(\bar{\tilde{p}})}{\partial \tilde{p}} \frac{\sigma_{\tilde{p}}}{\sqrt{N}} = \frac{20\sigma_{\tilde{p}}}{\bar{\tilde{p}} \ln(10)\sqrt{N}} \tag{15}$$

The accuracy of the final relative mean magnitude response in decibels (which in itself can be expressed as $\Delta\overline{L} = \overline{L}_u - \overline{L}_0$) is affected by the uncertainty of both components in the equation: measurements when driving at speed u ($\sigma_{\overline{L}_u}$) and the stationary measurements ($\sigma_{\overline{L}_0}$). Therefore, assuming random and independent processes give rise to the two uncertainties, they are added in quadrature to obtain the final uncertainty of the relative mean magnitudes for each frequency [75, Sec. 3.5]:

$$\sigma_{\Delta\overline{L}} = \sqrt{\sigma^2_{\overline{L}_u} + \sigma^2_{\overline{L}_0}} \tag{16}$$

The standard error formulated above may not capture all the random processes affecting the results, for example, wind velocity and background noise level fluctuations. Nonetheless, its small value, compared to the relative magnitude itself, would indicate that the statistical variability of the measurements is small, so the calculated mean could be considered a representative value of the true relative magnitude response.

5 Results

This section presents the results from two computer simulations of wind effect on sound propagation around two different model head cross-section geometries detailed in Chapter 3. It then presents the results obtained from the measurements outlined in Chapter 4. Finally, it discusses the agreement between the modelling and the measurement results.

5.1 Modelling Results

Due to the multiphysics nature of the aeroacoustics modelling, the following sections will firstly discuss the intermediate results from the CFD simulation before elaborating on the findings of the acoustic wave simulations.

5.1.1 CFD simulation

The first part of every numerical simulation included modelling the air velocity, pressure, and turbulent viscosity across the model domain and using them as background parameters in the acoustics simulations. Figure 7 and Figure 8 show examples of the modelled wind velocity from different modelling setups. The plots present time-averaged steady-state turbulent wind velocity fields. Figure 7 demonstrates two extrema of modelled wind speeds around a symmetrical circular object (6 m/s representing a moderate breeze in Figure 7a and 24 m/s classified as a strong gale in Figure 7b). The figures highlight the dependence of the shape of the wake region behind the head on the incoming wind velocity. The grey colour in the figures represents the flow speed at the inlet. The areas with lower average wind speed are blue, and the higher wind speeds are red. Although the colours correspond to

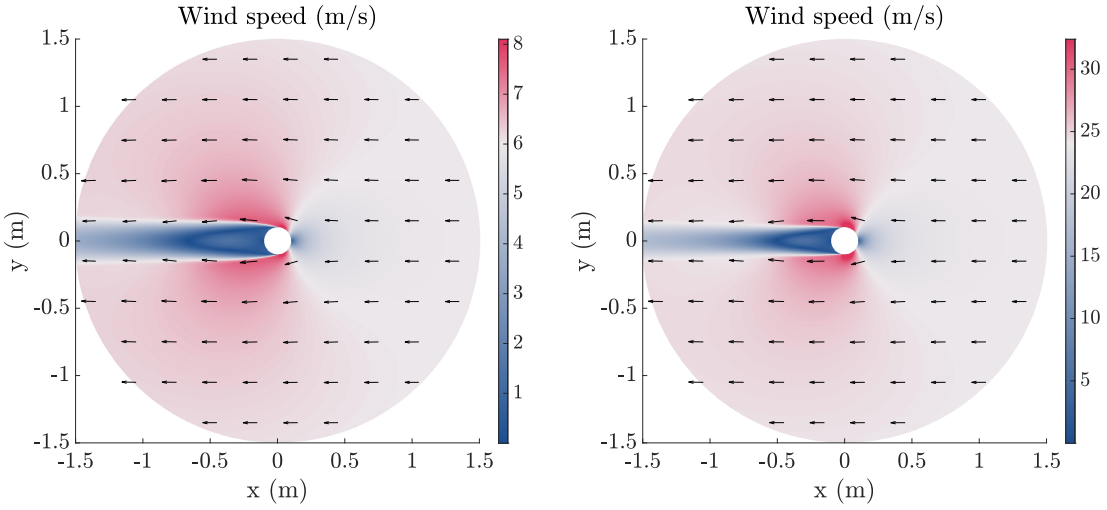

(a) *Inlet wind speed:* 6 m/s.

(b) *Inlet wind speed:* 24 m/s.

Figure 7: *Modelled wind velocity field of flow around a 2D circle.*

different absolute wind speeds, the maximum intensity of red corresponds to the speed 1.35 times higher than the inlet speed, so the relative wind speed profiles of the two plots are comparable.

The tailing wake in each simulation is highly turbulent. Due to the statistical averaging of the model, the wind speeds in this region approach zero due to the chaotic wind velocity field. The width of the wake region appears to be inversely proportional to the speed of the incoming wind: the shear layers, which separate each side of the wake region from the surrounding freestream flow, are more parallel and closer to each other in the case of a higher wind speed. At higher speed, the flow particles have more kinetic energy to overcome the pressure rise at the backside of the circle (discussed in Section 2.1.5), so they advance the boundary separation point further downstream, forming a narrower wake. For both wind inlet speeds, the flow accelerates in the region around the wake. The fluid particles reach the highest wind speeds when flowing past the side of the circle. These high-speed zones appear to be more concentrated around the proximity of the circle when the inlet speed is higher. Finally, a lower speed zone also forms in front of the circle, where the particles collide head-on with the solid object. However, the average speed gradients in this area are smaller than in the wake and do not form a visible 'tunnel', as is the case in the wake region. The flow profiles from the simulations generally follow the theoretical descriptions of subcritical and critical flow around a cylinder, discussed in Section 2.1.5.

For the asymmetrical 2D cross-section of the human head, the flow velocity field depends on the flow direction. Figure 8 compares the flow profiles around the cross-section of the head for 12 m/s wind at inlet in the upwind (Figure 8a) and the downwind (Figure 8b) case. The flow profile is similar to the previously discussed symmetric case. However, the downwind flow forms a wider wake region

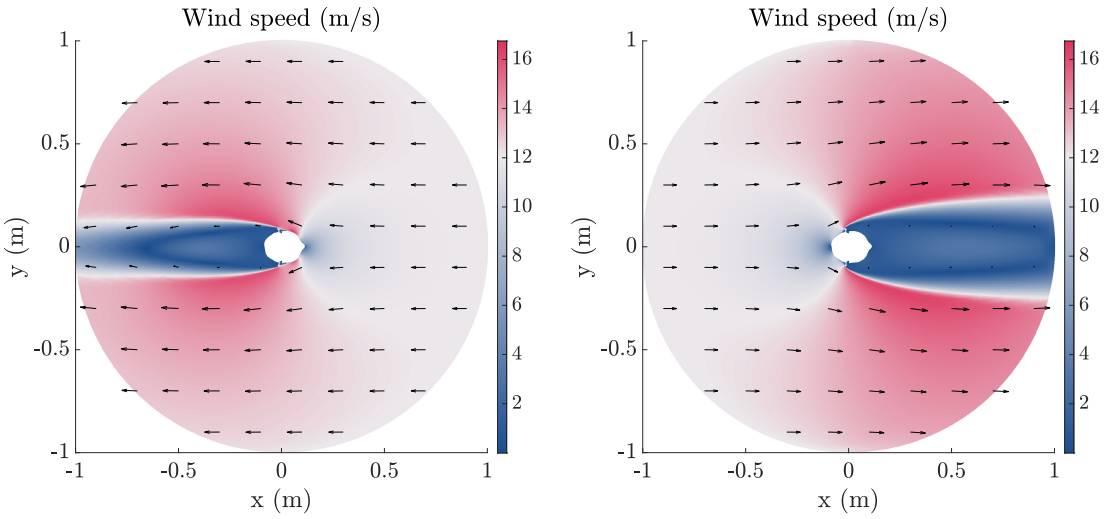

(a) *Upwind condition.* (b) *Downwind condition.*

Figure 8: *Modelled air flow around the 2D cross-section of the human head. The speed of flow at the inlet is 12 m/s.*

than the upwind flow. The visible protrusions, formed by the pinnae, result in a more discontinuous cross-section of the boundary, experienced by the flow in the downwind case, which results in an earlier boundary separation point. It widens the upstream low-flow-velocity area and pushes the high-velocity flow away from the boundary.

The second parameter mapped to the acoustics simulation domain from the CFD domain was the background pressure. Figure 9 shows two examples of the simulated relative pressure variations around the circle. The plots correspond to the airflow depicted in Figure 7. As expected, the relative pressure variations around the atmospheric pressure are much higher in the case of higher wind speeds (Figure 9b); however, the proportionality is non-linear and asymmetrical around the reference pressure. Therefore, the colour scales of the two plots are not synchronised and are not directly comparable. Still, a few common features between the plots can be highlighted. A higher pressure zone forms in front of the circle, where the approaching obstacle slows down the particle flow. The steepest pressure drop in both cases happens on the sides of the front part of the circle ('cheeks'), where the flow particles gain kinetic energy and accelerate around the circle. These pressure valleys, simulated by the model, agree with the theoretical predictions of flow around a cylinder, discussed in Section 2.1.5.

Similarly to the wind velocity, the relative pressure field around the 2D cross-section of the human head also depends on the direction of flow. Figure 10 compares the pressure fields around the cross-section for the upwind and the downwind case. These plots complement the velocity fields in Figure 7. The colour scale is synchronised between the two plots. The cross-section of the human head is more streamlined for the upwind flow, so the pressure decreases around the area of the 'cheeks', similarly to the flow around the circle. In the downwind case, however, the areas behind the

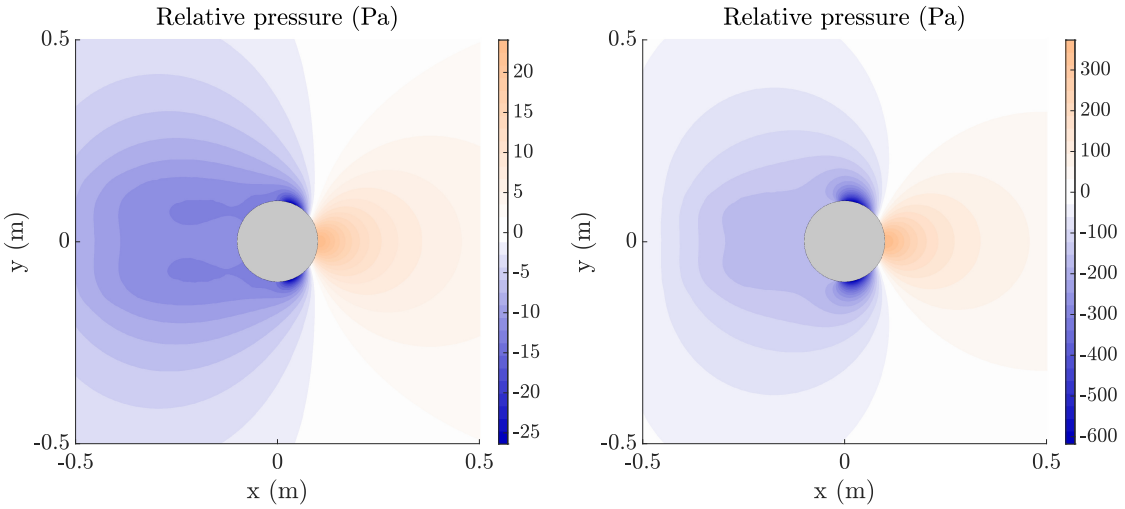

(a) *Wind speed at inlet: 6 m/s.* (b) *Wind speed at inlet: 24 m/s.*

Figure 9: *Modelled relative pressure variation around a 2D circle. Flow inlet is on the right. Reference pressure is 1 atmosphere (10^5 Pa).*

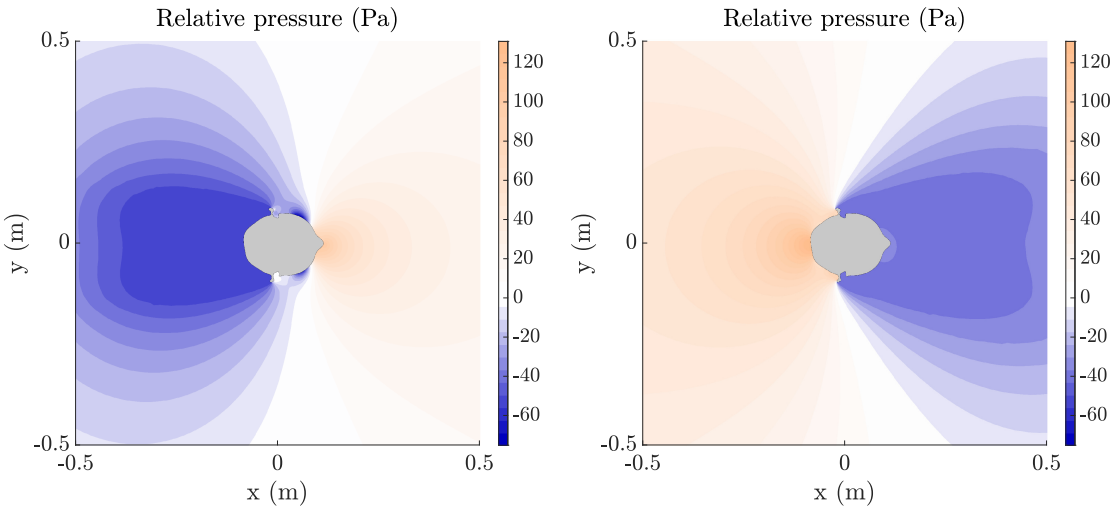

(a) *Upwind condition (right-to-left flow).* (b) *Downwind condition (left-to-right flow).*

Figure 10: *Modelled relative pressure variation around th 2D cross-section of the human head. Wind speed at inlet is 12 m/s. Reference pressure is 1 atmosphere (10^5 Pa).*

pinnae experience a pressure increase due to the sharp discontinuity, which traps the fluid particles and slows them down.

Finally, the turbulence effect on the acoustic wave propagation in the aeroacoustics simulations was accounted for by the effective dynamic viscosity of the airflow. Figure 11 and Figure 12 present examples of modelled turbulent dynamic viscosity for the simulations of the circle and the cross-section of the head, discussed previously. The colour scales between each pair of plots are synchronised. As expected, the strength of turbulence in the wake region is stronger when the flow speed is higher (Figure 11b). Furthermore, in the case of asymmetrical head, the wake region in the downwind scenario (Figure 12b) is wider and more turbulent than in the upwind scenario (Figure 12a). As noted previously, this effect is caused by the asymmetrical pinnae shape, which results in a more discontinuous cross-section for the downwind flow compared to the upwind one and consequently a more turbulent boundary separation for the downwind direction. The least turbulent regions appear to form upstream in front of the solid object.

In conclusion, the three modelled background flow parameters (flow velocity, pressure, and effective viscosity) depend on the flow speed at the inlet and, in the case of asymmetrical geometry, the direction of flow. Higher wind speeds cause higher velocity and pressure gradients around the boundary and a more turbulent but narrower wake. In addition, the discontinuities of the cross-section of the head for the downwind flow also lead to a more turbulent yet broader wake region downstream.

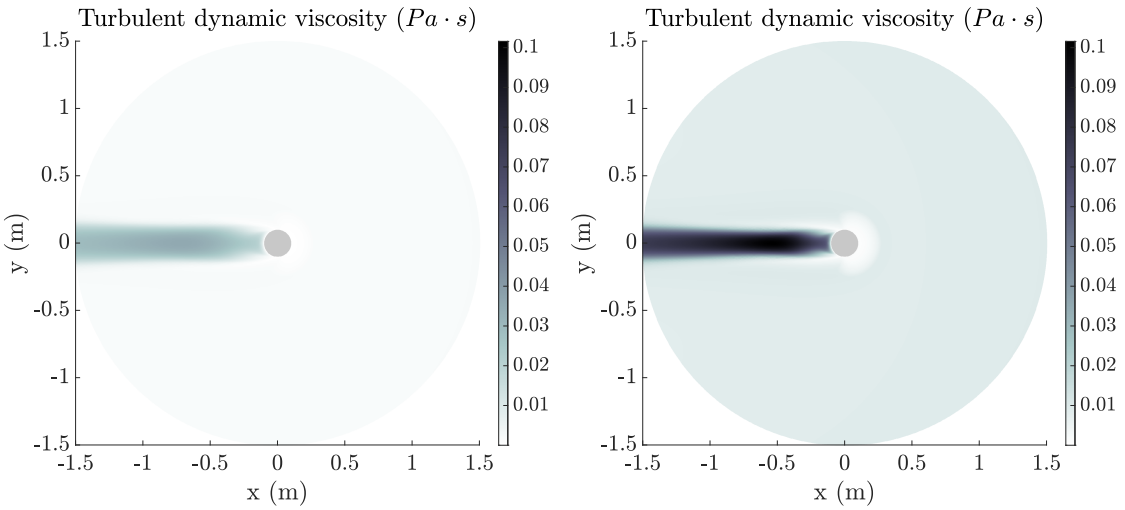

(a) *Wind speed at inlet: 6 m/s.* (b) *Wind speed at inlet: 24 m/s.*

Figure 11: *Modelled turbulent dynamic viscosity around a circle. Flow inlet is on the right.*

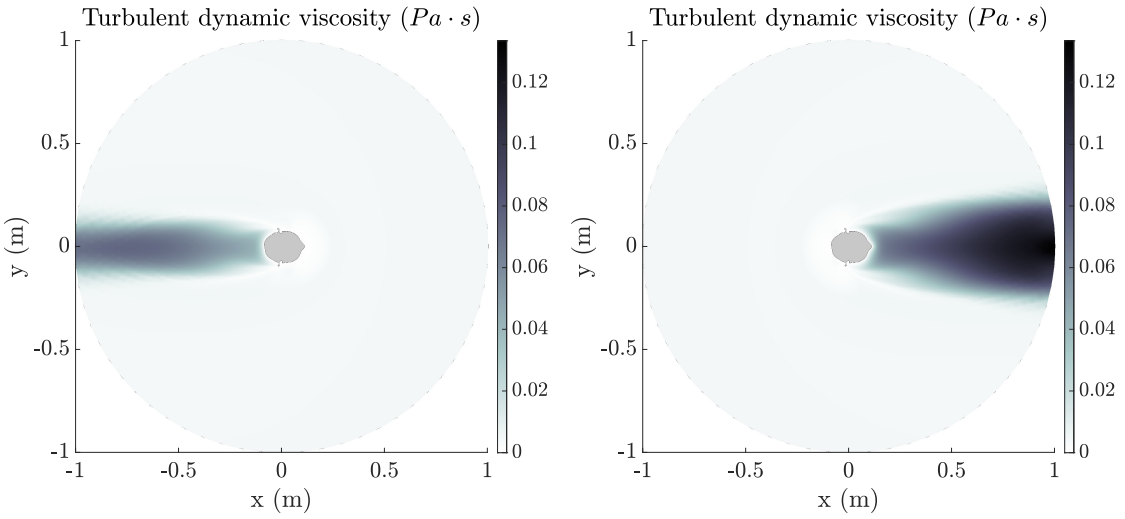

(a) *Upwind condition (right-to-left flow).* (b) *Downwind condition (left-to-right flow).*

Figure 12: *Modelled turbulent dynamic viscosity around the 2D cross-section of the human head. Wind speed at inlet is 12 m/s.*

5.1.2 Time-domain acoustics simulations

Time-domain acoustic wave simulations allow for monitoring the wave propagation in the modelling domain throughout the simulated time frame. This approach is beneficial for observing the changes in the speed of sound across the modelled domain. Furthermore, a free-field simulation can be easily ensured by windowing the simulation results up to the point when the sound wave reflects from the outer domain boundary. Frequency response is then obtained in the post-processing stage

from the modelled impulse responses. This section presents and discusses the results from the simulations of the 2D cross-section of the human head using time-dependent solvers.

A wide-frequency-band Gaussian pulse positioned at the location of the mouth (position S in Figure 5b) produces an impulse response at the location of the right ear canal (position R), which is affected by the prevailing wind. Figure 13a and Figure 13b show the recorded IRs at the source and receiver positions, respectively, for zero flow as well as 12 m/s upwind and downwind flows. At the location of the source, the impulses look almost identical, irrespective of the background flow. However, the shapes of the impulses deviate slightly by the time they reach the position of the ear.

Generally, the peaks in Figure 13b are shifted in time by approximately 0.48 ms

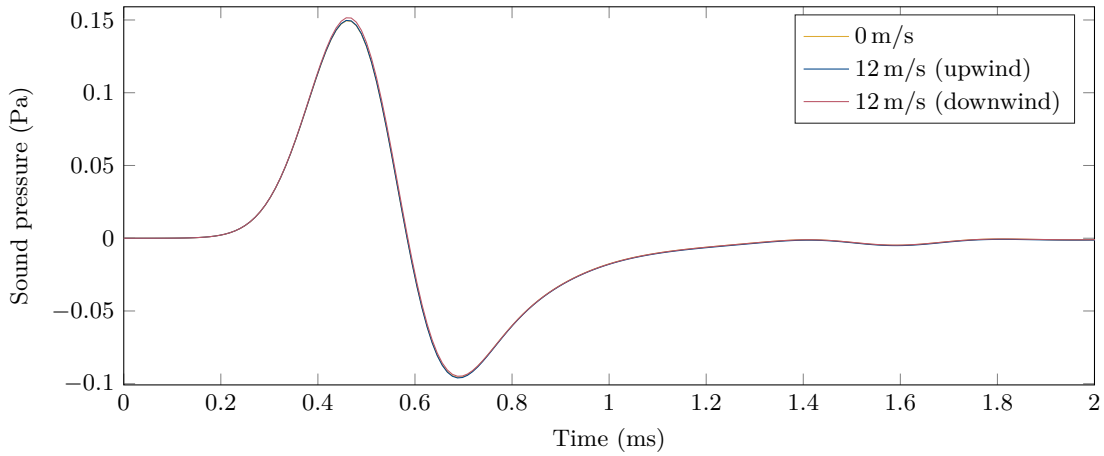

(a) *Sound pressure at source (mouth) position.*

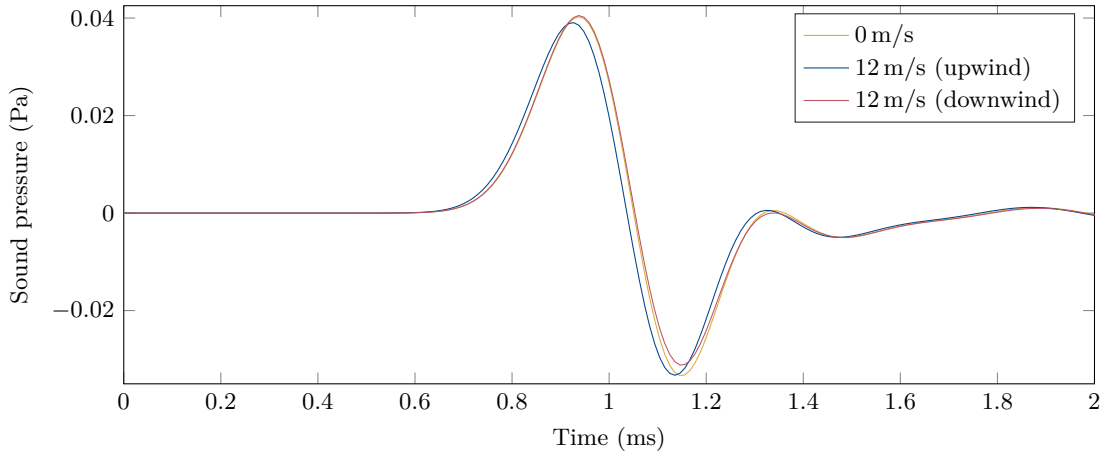

(b) *Sound pressure at right ear canal.*

Figure 13: *Simulated sound pressure variation in time domain for the condition of no background flow, 12 m/s upwind flow (mouth-to-ear direction) and 12 m/s downwind flow (ear-to-mouth direction). The simulated source was a Gaussian impulse at* $t = 0.5$ ms, $\sigma_t = 0.1$ ms.

compared to the IRs at the source (Figure 13a). To validate the modelled speed of sound, one could estimate that sound in this period would travel 0.48×10^{-3} s $\times$ 343 m/s $\approx$ 0.16 m. This estimate correctly correlates to a quarter of an elliptical arc-length of the human head with an approximate diameter of 20 cm: 20 cm $\times \pi/4 \approx$ 16 cm. Moreover, the amplitude of the impulse decreases more than threefold, from approximately 0.15 to 0.04, between the source and the receiver IRs. Because the simulation was created in a two-dimensional domain, the free-field wave distance attenuation is mathematically different from the three-dimensional space (the point source in the 2D domain behaves like an infinitely long line source in the 3D domain). However, the main interest of this study is the relative differences between the measured responses at the location of the ear rather than absolute sound pressures in each simulation, so the 2D simulation provides sufficient insight for this purpose.

Figure 13a also shows that in the upwind case (where the sound travels along the wind direction to reach the ears), the impulse is recorded slightly earlier than in the downwind or zero-flow scenarios. The timing of the impulse in the downwind and the zero-flow case is almost identical. Due to the pinnae, which shadow the wind in the downwind case (as seen in Figure 8b), the average wind speed along the path between the mouth to the ear canal is small. Therefore, the speed of sound next to the boundary is similar to the case of no flow.

For illustration, a complementary model was created to show the time-domain effects of the wind gradient on the propagation of single-frequency sound wave around the human head. The time-domain Gaussian pulse was replaced by a sinusoidal point source of the same Gaussian spatial distribution. The frequency of the sine wave was 250 Hz. The source was windowed by a Hann window to create a gradual initial onset and ensure model stability.

Figure 14 presents six snapshots from the simulations comparing 12 m/s upwind and downwind scenarios. The figure shows the propagation of the wavefronts throughout half a millisecond. The wavefronts were obtained from the simulated acoustic pressure field. The zero-crossing points in the time-domain were found by comparing the sign of the acoustic pressure between consecutive time steps at each node of the modelled mesh (in practice, the comparison was made between pressure values four-time-steps apart to collect a denser set of grid points around the zero-crossing condition). Additional post-processing was done to obtain the wavefront curve because the data from the simulation came as a sparse unordered set. For this purpose, a convex hull was computed from the zero-crossing points to extract an ordered outer boundary of the points. However, the density of data was not sufficient to draw a smooth curve. Therefore, a fourth-order uniform-subdivision spline curve was generated from the set of convex hull points using `spcrv` command in MATLAB [76]. The resulting wavefront exhibits certain processing artefacts, and the curves are not perfectly smooth. Moreover, convex hull computation is visually only accurate up to the point when the zero-crossing reaches the tips of the pinnae; afterwards, the wavefront curves inwards, so the processed shape is no longer accurate. However, the main interest of this study is the wave propagation between the mouth and the ears.

It is visible from Figure 14 that the prevailing background wind influences the

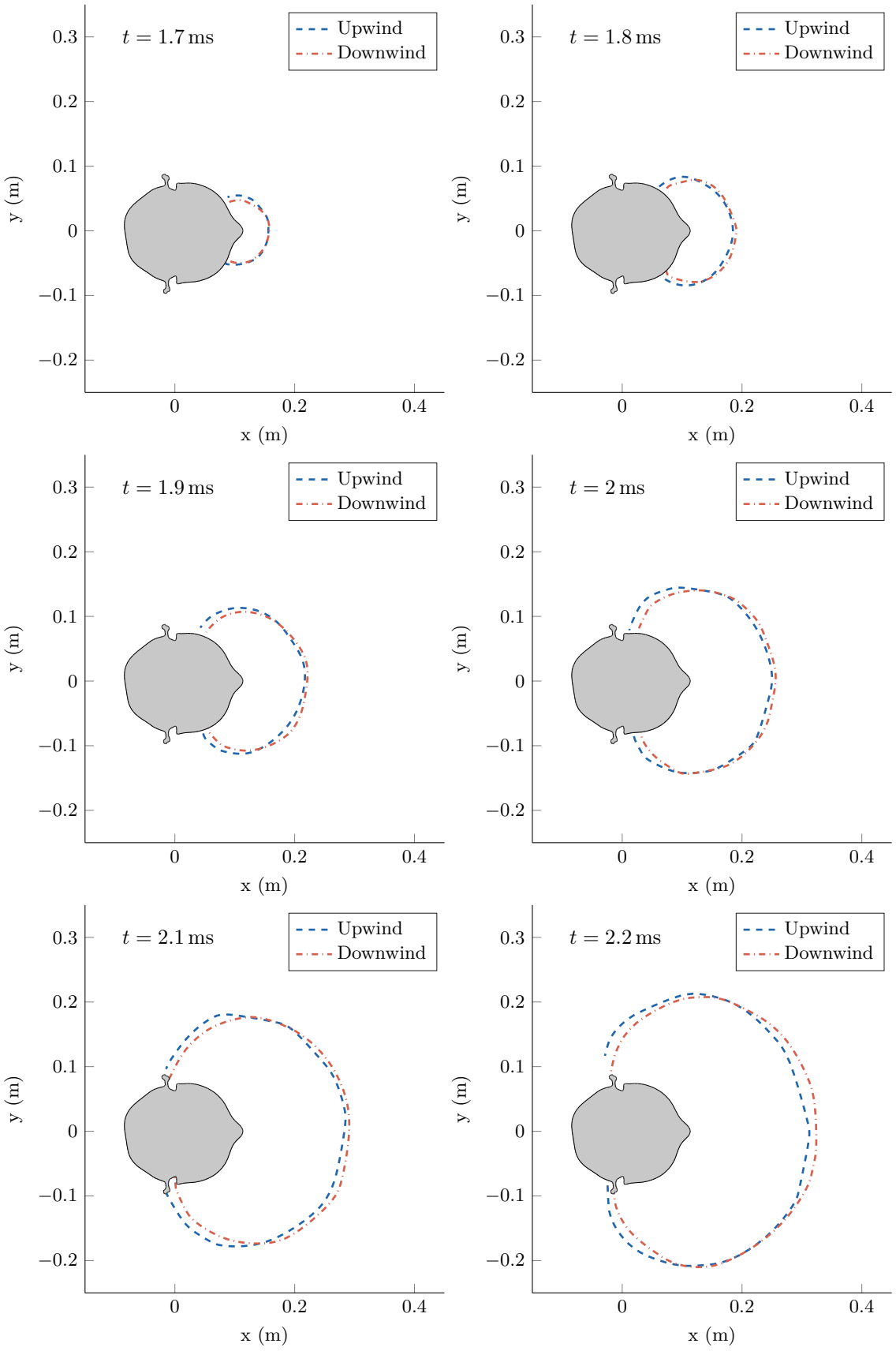

Figure 14: *Snapshots of simulated wavefront propagation of 250 Hz sine wave in 12 m/s wind. Upwind refers to right-to-left wind direction.*

effective speed of sound in an anisotropic fashion. In the upwind scenario, the wave travels along the wind direction when propagating from the mouth to the ears. It thus arrives at the ears faster than the wave travelling against the wind in the downwind case. On the other hand, the wave propagation forwards from the mouth slows down in the upwind case compared to the downwind case since the wave travels against the wind. This result is expected and agrees with the theory discussed in Section 2.2.1.

The recorded IRs, presented in Figure 13a, show a small difference in the peak amplitudes. It is easier to investigate the magnitude differences in the frequency domain. Therefore, example magnitude responses, calculated from IRs in Figure 13, are presented in Figure 15. The plots were created by computing absolute values of FFT from the time-domain signals. A one-sided Hann window was used to window the ends of the signals to ensure smooth signal decay to zero. They were also zero-padded to one second before calculating FFT to increase the frequency resolution of the frequency response (the original simulation length was around 5 ms to prevent the influence of reflections from the outer domain boundary).

The magnitude response of the source (Figure 15a) has a relatively broadband spectrum up to approximately 3 kHz. The reduction in magnitude response in higher frequencies is expected for a Gaussian impulse of finite width (the standard deviation of the simulated impulse was 0.1 ms). The responses are very similar for all background flow conditions, except for a slight low-frequency boost in the downwind scenario. As compared to the source position, the magnitude responses at the ear canal (Figure 15b) are lower by approximately 10 dB due to the distance attenuation. The low-frequency response appears to be affected by the background flow condition: the low frequencies are boosted by a few decibels in the downwind flow and attenuated in the upwind flow, compared to the no-flow scenario.

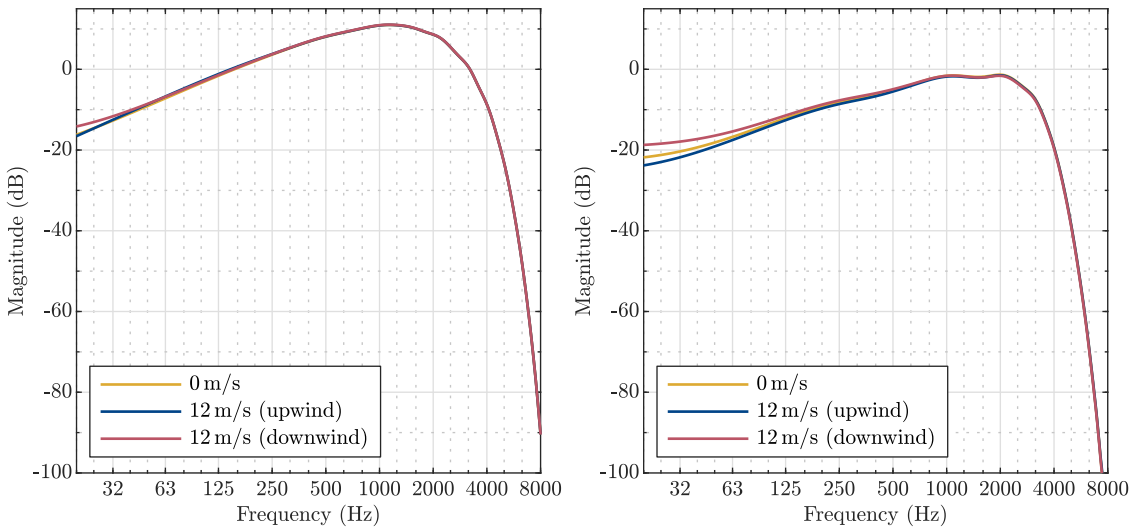

(a) *Source (mouth) position.* (b) *Right ear canal position.*

Figure 15: *Simulated magnitude responses, calculated from time-domain IRs (Figure 13). Minor ticks on the x-axis represent third-octave bands.*

However, the absolute magnitude responses, presented in Figure 15b are non-physical due to arbitrarily chosen modelled source amplitude and two-dimensional sound propagation. Instead, relative differences of magnitude responses provide more meaningful insight into the effect of wind. Figure 16 presents relative magnitude responses at the location of the right ear canal, normalised to the magnitude response of the zero-wind scenario. It covers wind velocities of 6 m/s, 12 m/s, and 24 m/s in both the downwind and the upwind direction (downwind velocities are represented by positive numbers to correspond to the flow along the direction of the positive x-axis, as in Figure 8b).

The magnitude response appears to depend on the velocity of the wind up to 1 kHz. The magnitude of the low-frequency sound is boosted in the downwind flow and attenuated in the upwind flow. The change is monotonous with the wind speed: 24 m/s upwind flow attenuates the sound the most, while the highest amplification happens in the 24 m/s downwind flow. The maximum level differences around the 125 Hz octave band (approximate fundamental frequency of a male voice) is of the order of a couple of decibels; however, the exact values are likely to be inaccurate due to the simplified modelling setup. The magnitude differences above 1 kHz appear to vanish. As seen in Figure 15, the absolute magnitude responses in the higher frequencies have a sharp roll-off, so the simulated sound source might not have enough signal energy in these higher frequencies to produce accurate results. Furthermore, the linear discretisation of the modelling mesh may contribute to unrealistic results

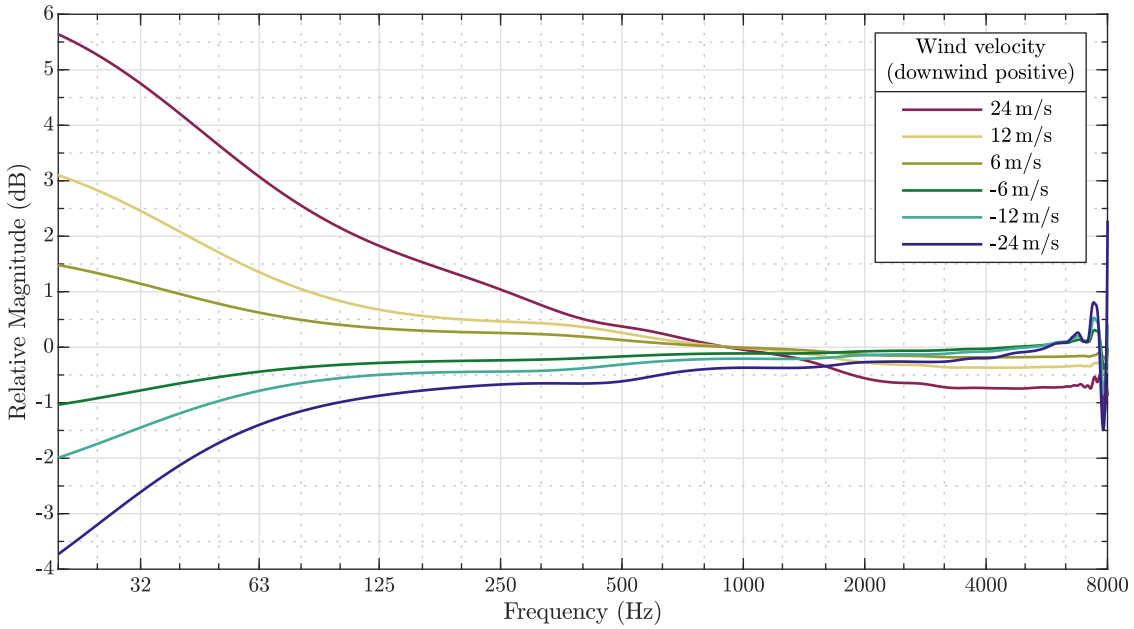

Figure 16: *Simulated relative magnitude responses at the position of the right ear canal for different wind velocities, obtained from the time-domain simulation. All responses were normalised to the magnitude response at zero-flow condition. Positive wind velocity represents downwind condition, i.e. ear-to-mouth direction of wind. Minor ticks on the x-axis represent third-octave bands.*

in the highest frequencies.

To sum up the time-domain acoustics simulation results, the models show that the sound propagation from the mouth to the ears is affected by the background airflow around the head. The speed of sound is affected by the air velocity; hence, in the upwind case, the sound from the mouth reaches the ears faster than in the downwind case. However, in the downwind scenario, the sound travelling to the ears is amplified in the low frequencies. The boost is of the order of a decibel and is dependent on the speed of the wind.

5.1.3 Frequency-domain acoustics simulation

To complement the results, obtained from the time-domain model, the results from the frequency-domain simulation are presented in this section. The geometry used in this simulation was circular (the CFD simulation for this geometry was presented in Figure 7, Figure 9, and Figure 11).

Complex frequency-domain pressure values were recorded at the location of the right ear (position R in Figure 4). The absolute values of the complex frequency responses were calculated and compared for different wind conditions. Figure 17 presents relative level differences of the simulated frequency responses, normalised to the results from the zero-flow simulation. Markers indicate the frequencies used in the simulation.

The results, presented in Figure 17, correlate well with the results from the time-domain simulation (Figure 16). The magnitude response appears to depend on

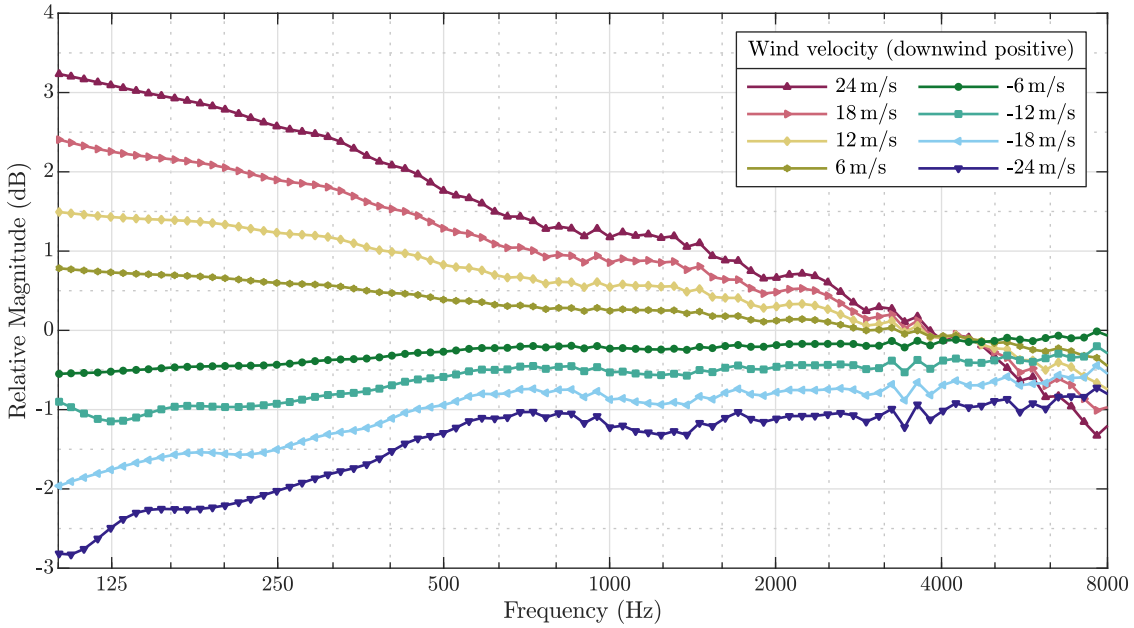

Figure 17: *Simulated relative frequency-domain results at the right ear position for different wind velocities. Magnitudes were normalised to the magnitude response at zero-flow condition. Minor ticks on the x-axis represent third-octave bands.*

the background flow in the same manner as found previously: background downwind flow amplifies the sound, especially in the lower frequency range, while upwind flow attenuates the sound. The change is again monotonous with the wind speed. The results from the frequency-domain study support the previous finding that the effect is the strongest in the lowest frequency range and decreases in the higher frequencies. Compared to the time-domain simulation, the level differences in the frequency-domain study are consistent up to a higher frequency, around 4 kHz.

Frequency-domain simulation allows for comparing the acoustic pressure fields across the whole modelling domain for each modelled frequency. Figure 18 presents level differences of simulated absolute acoustic pressure fields around the circle for three modelled frequencies at 12 m/s background flow. Each pressure field was normalised to the simulated zero-flow pressure field. The lowest frequency represented is 292 Hz (its wavelength is slightly smaller than the domain radius). Comparisons of even lower frequency results displayed modelling instabilities in the shear layer, potentially because their wavelengths were longer than the modelling domain, so they are not presented here. Other frequencies plotted in the figure are 500 Hz and 1001 Hz. In all the downwind scenarios (Figure 18b), the pressure field was mirrored along the x-axis to ease visual comparison.

At the lowest frequency, the dimensions of the circular obstacle are small compared to the wavelength of the sound wave (0.2 m diameter compared to 1.17 m wavelength of 292 Hz wave). In this case, the acoustic pressure field is generally boosted in the areas where the sound propagation direction opposes the background flow and attenuated in the areas where the sound travels in the same direction as the flow. The amplification (or attenuation) of the sound pressure directly in front of the speaker is around 0.5 dB. The observation is in line with the upstream amplification phenomenon, discussed in Section 2.2.1, which predicts 1.2 dB difference for a plane wave, travelling against the wind versus with the wind. The similarity between the plotted acoustic pressure difference field and the shape of the wake region of the background flow (Figure 7) appears to be small. The most significant differences in the sound pressure magnitudes are concentrated on the sides of the circle around the location of the ears. In this region, the wind speed is the highest, and the speed gradients are steep. In the downwind scenario, the sound wave propagates against the wind in this area and gets amplified. In the upwind scenario, the wave propagating with the wind is attenuated. The result agrees with the theory of energy exchange for sound travelling in a sheared flow: the sound waves gain energy when propagating along the negative flow gradients and lose energy along the positive flow gradients.

For the 500 Hz acoustic wave, the division line between the negative and the positive relative magnitudes is similar to the one visible in 292 Hz plots, but it is moved slightly further against the flow direction. At this frequency, higher pressure level zones within the wake regions emerge in both wind directions. The negative relative pressure level zones surround these areas. However, sound amplification is still higher in the general regions where the sound travels against the flow than in the downstream wake regions. The most significant magnitude differences remain around the location of the ears, as in the lower frequency.

At 1001 Hz, the wavelength of the acoustic wave (0.34 m) approaches the diameter

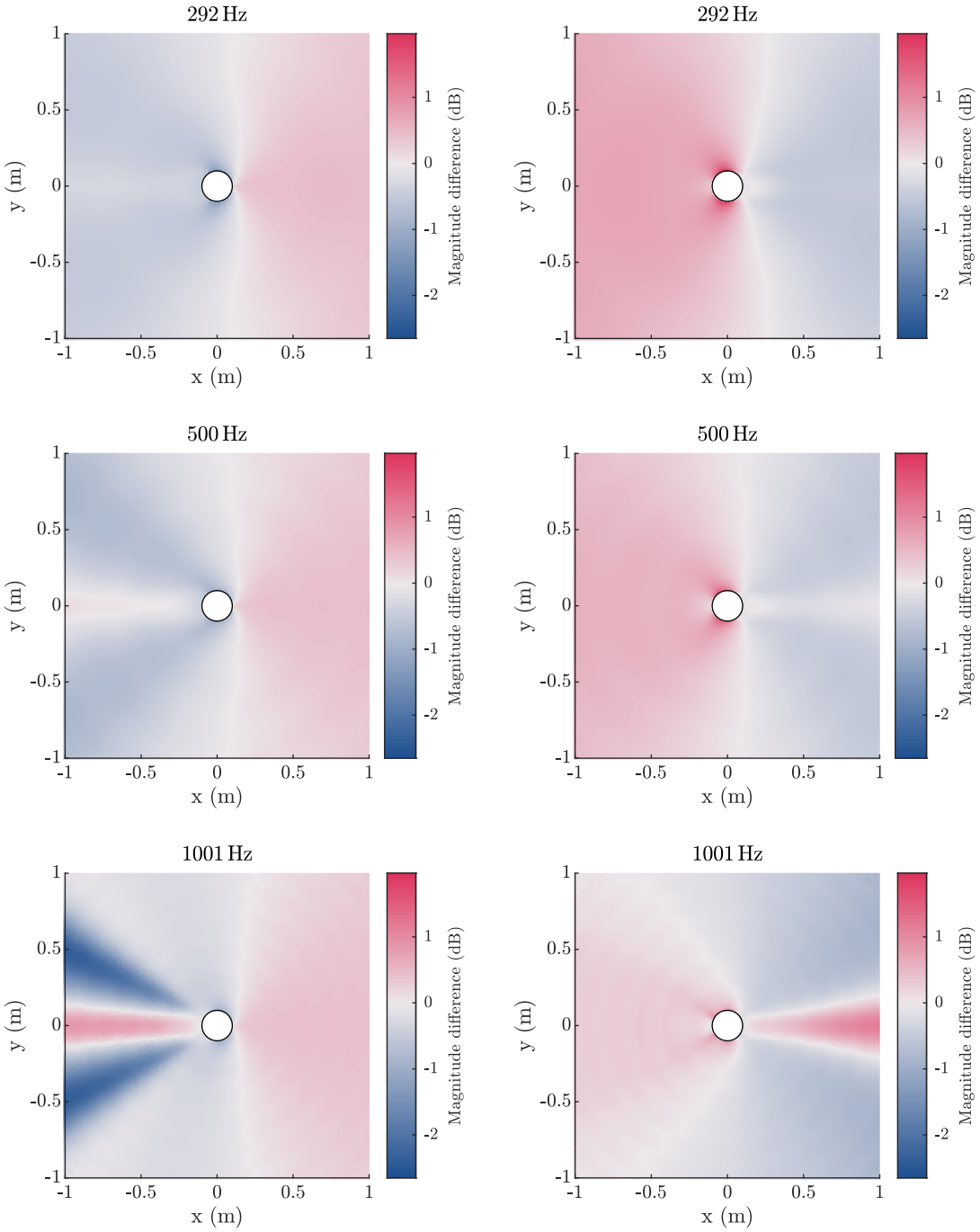

(a) *Upwind scenario (right-to-left direction of wind).*

(b) *Downwind scenario (left-to-right direction of wind).*

Figure 18: *Magnitude differences of simulated frequency-domain pressure fields. The comparison was done between the simulation with 12 m/s wind speed at the inlet and zero-flow simulation. Colour scales were synchronised between the plots.*

of the circle and the width of the wake region. Therefore, the influence of the obstacle and the exact shape of the background flow field appears to be greater than in the lower frequencies. The sound pressure is projected outwards by the wake region, surrounded by lower magnitudes. Sound propagation for this and higher frequencies appear to behave more similarly to the ray approximation, presented in Section 2.2.1. For the sound waves propagating in the wake with lower background flow speed, the shear layer partly reflects and partly refracts the sound inward, creating the acoustic waveguide, visible in the plots. Although the upstream amplification of the opposing flow still magnifies the forward-propagating sound in the upwind scenario, the waveguide of the wake downstream appears to provide a more substantial boost at this and higher frequencies. However, the acoustic amplification (or attenuation) around the ears due to the wind is diminished. The directivity pattern at 1000 Hz shows a good correlation with the results presented in [14, Fig. 3, 5], where outward voice directivity was modelled for frequencies from 1000 Hz to 8000 Hz.

To summarise, the pressure field difference plots complement the comparisons obtained from the pressure probes at the location of the ears in frequency (Figure 17) and time (Figure 15) domains. They show the magnitude boost around the area of the ears in the downwind flow scenario and attenuation in the same area in the upwind scenario. The effect on sound pressure level appears to be frequency-dependent, and the most prominent variations are present for the lowest frequencies. The comparisons also confirm the theory of upstream amplification (downstream attenuation) and previous findings of the directivity of the voice in the background flow and hence validate the simulations.

5.2 Measurement Results

Measurements of wind influence on sound propagation around a cross-section of the head were conducted according to the methodology presented in Chapter 4. Below, the wind speed measurements are summarised, a typical mean magnitude response from one of the measurements presented, and relative magnitude responses at different wind conditions compared.

Table 2 presents means and standard deviations of wind speeds, which were calculated from the measurement segments, selected for the mean magnitude response calculations. It reports the wind data for each combination of the speaker direction and the driving speed measured. The number of measurement segments used in the analysis differed for each scenario (indicated in column N of the table). This variation was caused by the wind stability criteria imposed in the data analysis stage and a shorter measurement length when higher driving speeds were used. Each driving condition had a set of stationary measurements associated with it, taken immediately before and after each drive, so averaged values of each stationary wind measurements are reported alongside the driving scenarios in the same table. Unlike in the driving case, where the primary wind direction was assumed to be reasonably steady against the drive direction, wind direction during the stationary measurements was unpredictable. The speed averaging process did not take the directionality into account. Therefore, direct wind speed comparisons between the

Table 2: *Summary of mean measured wind speeds and standard deviations over the measurement segments used in the magnitude response analysis. Each averaging was done over N segments without taking the wind direction into account.*

Speaker direction	Driving			Stationary		
	$\overline{u}_{wind}$ (m/s)	σ_u (m/s)	N	$\overline{u}_{wind}$ (m/s)	σ_u (m/s)	N
0° (upwind)	6.3	0.5	36	0.3	0.8	10
	11.7	0.7	27	2.4	0.0	2
	18.0	0.6	16	1.1	0.9	18
	23.3	0.8	8	0.8	0.8	9
180° (downwind)	6.5	0.7	35	2.2	0.1	3
	12.0	1.0	22	1.9	0.4	5
	18.1	1.0	12	1.5	0.8	6
	23.5	0.4	4	1.4	1.0	4

driving and the associated stationary conditions cannot be made. Instead, stationary wind measurements indicate the prevailing wind condition and possible biases of the measurements.

Mean wind speeds of the chosen driving segments agree with the desired and modelled wind speeds of 6 m/s, 12 m/s, 18 m/s, and 24 m/s within 0.7 m/s range. Their standard deviations are within the range of 0.4 m/s to 1.0 m/s. The wind speeds of the stationary measurements reach a maximum of 2.4 m/s, which is just below the limit of 2.5 m/s, imposed on the stationary measurements in the data analysis stage. The standard deviation of the stationary measurements is less than or equal to 1.0 m/s. On average, the prevailing background wind in the downwind measurements is higher than in the upwind ones. A visual review of the recorded footage of the weather vane revealed that the dominant wind in the first half of the measurements (0° direction) was westerly and north-westerly. In the second half of the measurements (180° direction), the wind changed to a predominantly south-westerly and south wind (the direction of the drive was east-to-west).

The chosen time-domain measurement segments at the position of the ear were converted to the frequency domain, and their magnitudes averaged for each driving condition. Figure 19 shows an example of mean magnitude response for the measurement in the wind and an associated mean stationary measurement. Mean background noise responses and the estimated noise floors are also plotted on the figures. The multitone peaks, which satisfy the 20 dB SNR criteria, are marked by red crosses. Additionally, red dots represent the data used in the averaging process and indicate the spread of the measurements.

The magnitude response plotted in Figure 19a represents one of the two scenarios with the highest wind speed. Therefore, it demonstrates the highest recorded background noise profile. The envelope of the background noise across all the measurements was of a similar low-pass nature with an approximate negative slope of 10 dB per octave but lower in overall level for slower driving speeds. Due to the high

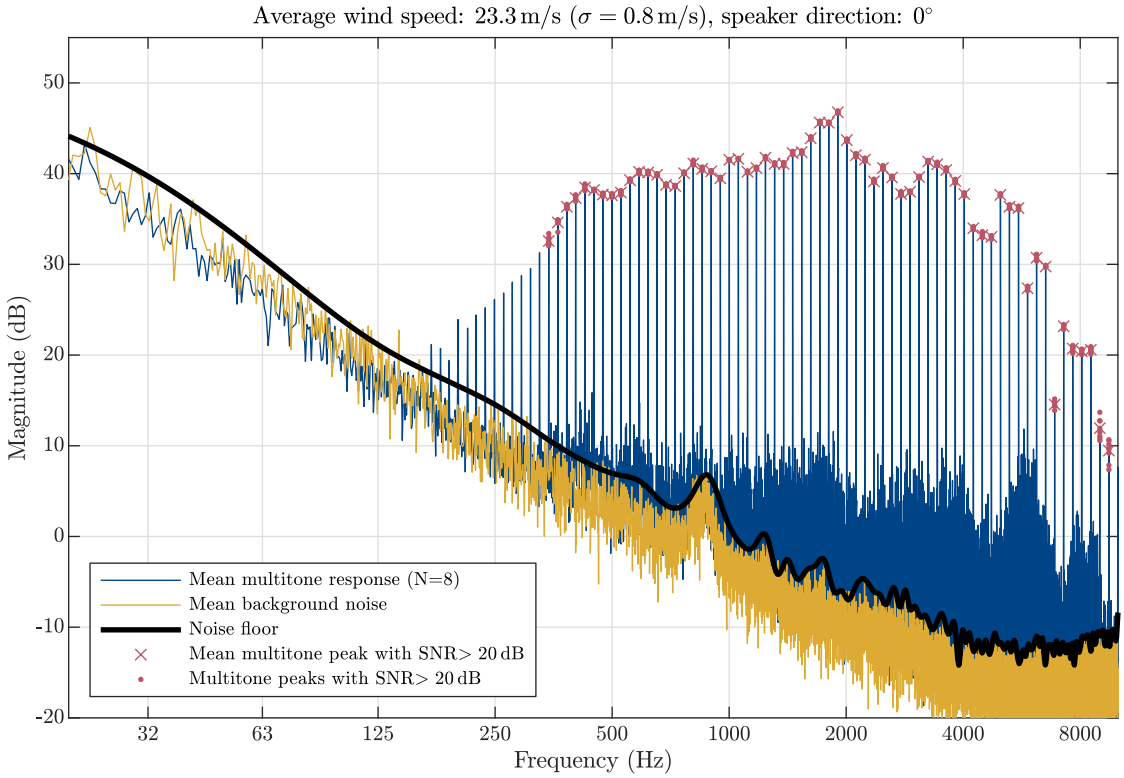

(a) *Averaged magnitude response for an upwind driving condition*

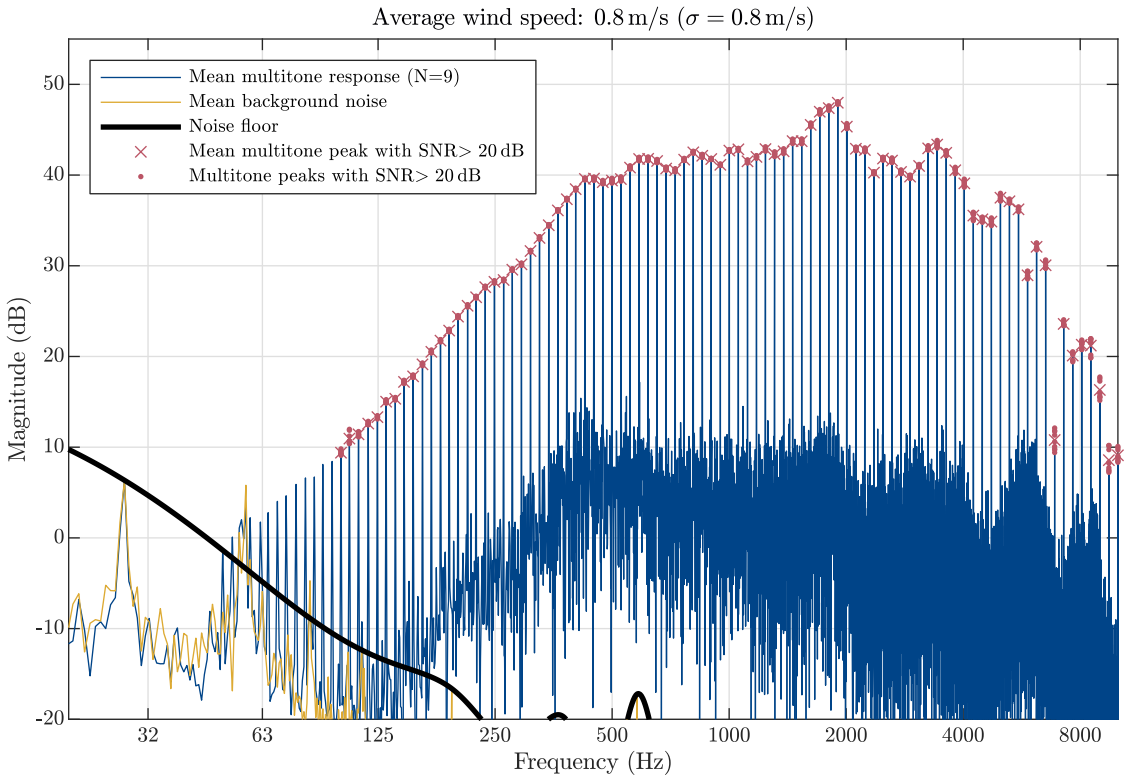

(b) *Corresponding averaged magnitude response for a stationary condition.*

Figure 19: *An example of mean measured magnitude responses and background noise floor for upwind direction and its associated no-wind response. Red dots indicate the spread of individual peaks, used in the averaging process and the crosses mark their mean value.*

output power of the compression driver and the low-pass nature of the wind-induced noise, multitone peaks as low as 350 Hz achieved the desired SNR criteria even in the highest wind speeds measured. Frequencies as low as 130 Hz in the case of 6 m/s wind had a satisfactory SNR. At the highest wind speeds, the background noise had a peak in the magnitude response around 800 Hz, which was heard as a whistling sound during the measurements. However, the magnitude response of the speaker in this frequency range highly surpassed the desired SNR, so the whistle did not affect the measurement results.

The comparison between the magnitude responses at the position of the ear across different measurement scenarios was made in the frequency bins with sufficient SNR. Due to the high density of tones, the sampled frequency response was assumed to represent the underlying broadband response. Relative wind-dependent magnitude responses, normalised to their respective stationary responses, are presented in Figure 20. Additionally, the data at sample multitone frequencies and the corresponding SEMs are summarised in Appendix A. All the plotted and tabulated data satisfy 20 dB SNR criteria; hence, the higher wind speed measurements lack data points in the lowest frequencies.

Generally, in the frequency range up to approximately 4 kHz, the magnitude

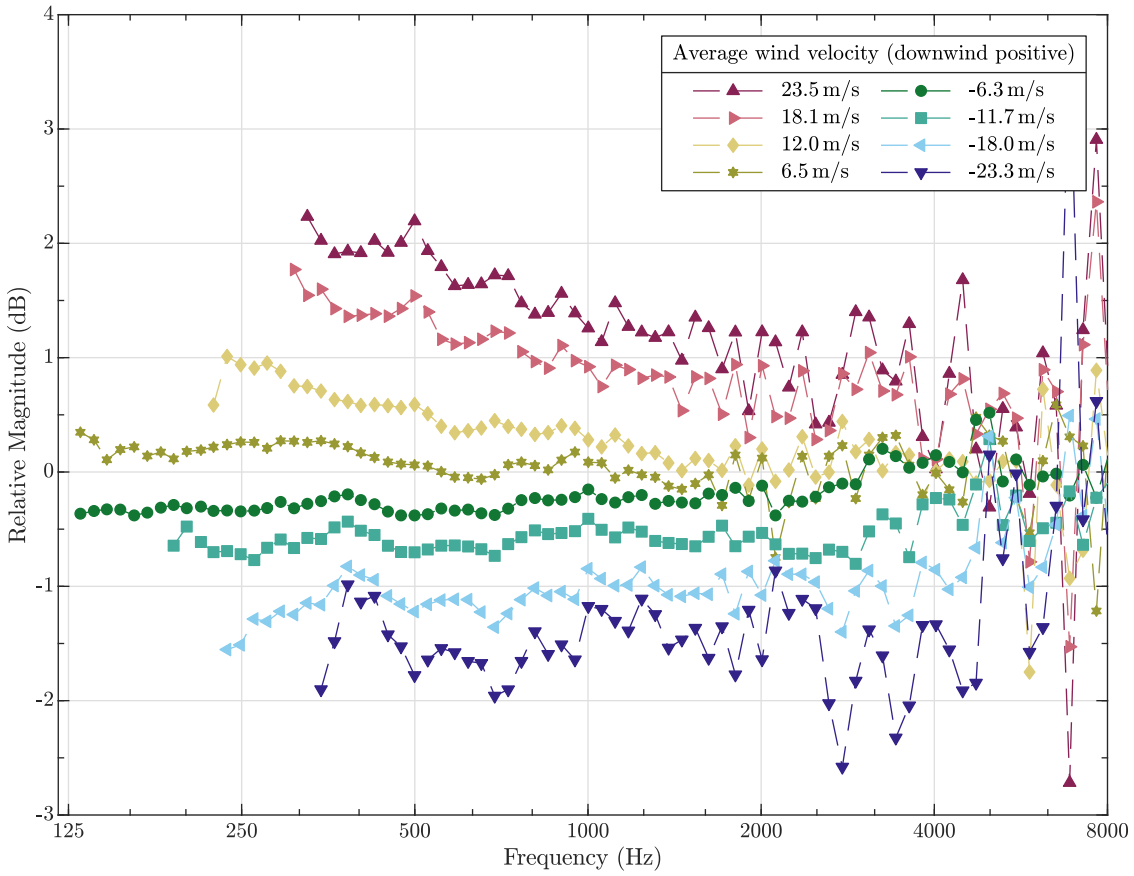

Figure 20: *Measured relative magnitude responses at the position of the ear for different wind velocities, normalised to respective measured stationary responses.*

response appears to depend on the wind velocity in a monotonous fashion. Strong upwind flow attenuates while downwind flow amplifies the sound. The effect is the strongest in the lowest frequencies, with approximately 2 dB sound amplification around 500 Hz in 23.5 m/s downwind flow and an attenuation just short of 2 dB in 23.3 m/s upwind flow. The responses in the frequencies above 4 kHz lose this consistent behaviour. However, in the higher frequency range, the size of the wavelengths (the wavelength of a 4 kHz wave is approximately 0.09 m) are comparable to or smaller than the radius of the cylinder (0.1 m) and the distance between the driver and the speaker (0.16 m), so small variations in microphone positioning might affect the resulting magnitude response.

For the measurements in the smallest wind speeds (approx. 6 m/s) the statistical uncertainties of the relative magnitudes upwind (Table A1) and downwind (Table A2) are below or equal to 0.3 dB. The magnitude differences in these wind speeds exceed the uncertainties only in the lowest frequency range (up to 1240 Hz for the sample upwind data and up to 403 Hz for the sample downwind measurements). However, as the wind speed increases, the differences in measured magnitudes are larger than their uncertainties for a broader range of frequencies. For the highest measured wind speeds in either direction, relative magnitudes in all frequency bands up to 3081 Hz are larger than their uncertainties.

Although the statistical uncertainties are higher than the mean measured relative magnitudes for some frequencies (especially for lower wind speeds), the results from the measurements show a clear trend that the recorded magnitude spectra depend on the speed and direction of the wind and that the effect is the strongest in the lowest frequency range.

5.3 Discussion

Relative magnitude spectra for the two simulations and the measurements, presented in Figure 16, Figure 17, and Figure 20, demonstrate a similar trend: for a sound propagating externally from the mouth, the sound pressure at the location of the ears increases in the presence of the downwind flow (i.e. when the sound propagates against the flow to reach the ears). Conversely, it is attenuated in the upwind flow (i.e. when the sound propagation to the ears coincides with the general direction of the flow). The amplification and the attenuation are monotonous with the wind speed: the highest amplification is recorded in the 24 m/s downwind flow, while the highest attenuation is observed in the 24 m/s upwind flow. The effect also depends on the frequency: it is the strongest in the lowest frequency range and diminishes in the higher frequencies. The critical frequency (above which the effect vanishes) is around 3-4 kHz in the measurements and the circular geometry model. For the model of the cross-section of the head, it is around 1 kHz. The wavelengths of the sound at higher frequencies are comparable or shorter than the dimensions of the head; therefore, the recorded and simulated responses are more sensitive to the exact location of the ear probes, the geometry of the system, and more minor details of the flow profile. Lower critical frequency for the cross-section of the head could be a result of a more complicated geometry used, where the sound interacts with the pinnae

and the ear canal and the discretisation of the model is less reliable. Furthermore, the time-domain simulation used for the cross-section of the head is typically less stable than the frequency-domain simulation used for the circular model.

In the frequency region, in which the sound is amplified or attenuated by the flow, the relative magnitude differences generally vary in a range of 0 dB to 2 dB. For example, at 500 Hz and 12 m/s background wind, the time-domain model produces approximately symmetric 0.3 dB attenuation or boost, depending on the wind direction. The frequency-domain simulation predicts approx. 0.6 dB attenuation for the upwind and 0.8 dB amplification for the downwind case. The measurements show 0.6-0.7 dB effect for the same frequency. These results generally agree with the upstream amplification phenomenon in low-Mach flows, which predicts 1.2 dB difference for plane waves in the upstream versus the downstream flow. Furthermore, the analysis of the simulated pressure field at that frequency (Figure 18) reveals a broader agreement with the theory of energy exchange from the opposing background flow velocity gradient to the acoustic waves. The same pressure field plots show that for higher frequencies, the shear layers of the wake region demonstrate waveguiding properties, as predicted by ray-acoustics approximation and confirmed in the previous study on voice directivity in the wind.

In the case of speech, the predicted phenomenon affect self-audition of the lowest frequency range: the strength of the fundamental frequency of the voice, the first and potentially the second formant of some phonemes. As discussed in Sec. 2.3.1, this frequency range is significant in the vowel perception. Furthermore, based on the studies presented in Sec. 2.4, the air-conducted contribution is typically higher in this range than the bone-conducted part of self-audition for most vowels and some consonants. Therefore, the frequency-dependent change in the strength of air-conducted voice due to the wind around the head may lead to a perceived voice colouration: in stronger winds, one's own voice might sound louder and 'deeper' when speaking downwind, compared to upwind.

6 Summary

This thesis investigated the impact of wind around the human head on the external sound propagation from the mouth to the ears. The effect was analysed for winds of 6 m/s to 24 m/s in the upwind (incident on the face) and the downwind (incident on the back) directions on the horizontal plane using computer simulations and physical measurements.

The models for a two-dimensional approximation of a cross-section of the human head were created using the FEM in COMSOL Multiphysics® software. The simulations used the RANS-based SST turbulence model to predict the stationary averaged background flow; then, the flow velocity, pressure, and effective viscosity fields were used as background parameters for the LNS acoustics simulation. A Gaussian pulse imitated the external sound propagation of the mouth. The simulated acoustic pressure field was recorded at the position of the ears. Both frequency and time–domain simulations were used. For the measurements, airflow around a tall cylinder approximated the two-dimensional flow around a horizontal cross-section of the human head. A compression driver, installed in the middle of the cylinder, acted as an artificial mouth and microphones, attached on the sides, recorded the response at the position of the ears. The measurement rig was placed on the roof of a van. The vehicle was driven on an airfield to imitate the airflow in the opposite direction. A dense logarithmically-spaced multitone signal was used in the measurements, and the resulting frequency-domain magnitude spectra were analysed at the multitone frequencies. The magnitude spectrum in the zero-flow (stationary) condition was also measured and simulated. The stationary magnitude responses were subtracted (in decibels) from the respective responses in the wind to obtain the relative spectra for each wind velocity.

The simulations and the measurements provide evidence that upwind flow attenuates while the downwind flow amplifies the low- and mid-frequency-range sound, which propagates externally from the mouth to the ears. The findings agree with the upstream amplification phenomena and the theory on energy exchange in a sheared flow. As a result, the low-frequency features of one's own voice when speaking downwind might be perceptually increased relative to the zero-wind or upwind scenario due to the importance of air-conducted contribution to the self-audition at this frequency range.

The study was limited to the horizontal effects of the airflow and a two-dimensional simplified geometry. In the three-dimensional scenario of wind interacting with a complex geometry of the head, the strength and the frequency range of the effect might differ. However, the main findings are believed to be similar for the 3D geometry as well.

The simulations could be extended to a more complex 3D domain using a more sophisticated modelling setup and computing resources to produce convergent solvers. The measurements could also be run on a head-and-torso simulator with a built-in artificial mouth and ears. Furthermore, a listening test could be devised to assess the perceptual strength of the effect for the human subjects. These considerations are left as topics for future research.

References

[1] G. von Békésy, "Structure of the Middle Ear and Hearing of the Voice by Bone Conduction," in *Experiments in Hearing*, Acoustical Society of America, 1960, ch. 6, pp. 181–203, ISBN: 0-88318-630-6.

[2] H. Brumm and S. A. Zollinger, "The evolution of the Lombard effect : 100 years of psychoacoustic research," *Behaviour*, vol. 148, no. 11/13, pp. 1173–1198, 2011. [Online]. Available: https://www.jstor.org/stable/41445240.

[3] U. Ingård, "A Review of the Influence of Meteorological Conditions on Sound Propagation," *Journal of the Acoustical Society of America*, vol. 25, no. 3, pp. 405–411, 1953. DOI: 10.1121/1.1907055.

[4] J. E. Piercy, T. F. Embleton, and L. C. Sutherland, *Review of noise propagation in the atmosphere*, 1977. DOI: 10.1121/1.381455.

[5] T. F. W. Embleton, "Tutorial on sound propagation outdoors," *The Journal of the Acoustical Society of America*, vol. 100, no. 31, pp. 31–48, Jul. 1996, ISSN: 0001-4966. DOI: 10.1121/1.415879.

[6] S. Karabasov, L. Ayton, X. Wu, and M. Afsar, "Advances in aeroacoustics research: Recent developments and perspectives," *Philosophical Transactions of the Royal Society A: Mathematical, Physical and Engineering Sciences*, vol. 377, no. 2159, 2019, ISSN: 1364503X. DOI: 10.1098/rsta.2019.0390.

[7] S. Kephalopoulos, M. Paviotti, and F. Anfosso-Lédée, "Common noise assessment methods in Europe (CNOSSOS-EU)," European Commission, Tech. Rep., 2012. DOI: 10.2788/31776.

[8] B. Plovsing, "Nord2000. Comprehensive Outdoor Sound Propagation Model. Part 2: Propagation in an Atmosphere with Refraction," Delta Acoustics and Electronics, Tech. Rep., 2006, pp. 1–127.

[9] L. Bertsch, M. Snellen, L. Enghardt, and C. Hillenherms, "Aircraft noise generation and assessment: executive summary," *CEAS Aeronautical Journal*, vol. 10, no. 1, pp. 3–9, 2019, ISSN: 18695590. DOI: 10.1007/s13272-019-00384-3.

[10] T. Sassa, T. Sato, and S. Yatsui, "Numerical analysis of aerodynamic noise radiation from a high-speed train surface," *Journal of Sound and Vibration*, vol. 247, no. 3, pp. 407–416, Oct. 2001, ISSN: 0022460X. DOI: 10.1006/jsvi.2001.3773.

[11] X. Zhang, "The directivity of railway noise at different speeds," *Journal of Sound and Vibration*, vol. 329, no. 25, pp. 5273–5288, 2010, ISSN: 0022460X. DOI: 10.1016/j.jsv.2010.07.003.

[12] H. H. Hubbard and K. P. Shepherd, "Aeroacoustics of large wind turbines," *The Journal of the Acoustical Society of America*, vol. 89, no. 6, pp. 2495–2508, 1991, ISSN: 0001-4966. DOI: 10.1121/1.401021.

[13] D. Heimann and A. Englberger, "3D-simulation of sound propagation through the wake of a wind turbine: Impact of the diurnal variability," *Applied Acoustics*, vol. 141, pp. 393–402, Dec. 2018, ISSN: 0003682X. DOI: 10.1016/j.apacoust.2018.06.005.

[14] V. Pulkki, T. Lähivaara, and I. Huhtakallio, "Effects of flow gradients on directional radiation of human voice," *The Journal of the Acoustical Society of America*, vol. 143, no. 2, pp. 1173–1181, 2018, ISSN: 0001-4966. DOI: 10.1121/1.5025063.

[15] I. Huhtakallio, "Effects of wind on speech production, transmission and perception," M.S. thesis, Aalto University, 2014. [Online]. Available: http://urn.fi/URN:NBN:fi:aalto-201403061526.

[16] R. E. Berg, *Sound*, 2020. [Online]. Available: https://www.britannica.com/science/sound-physics.

[17] The Editors of Encyclopaedia Britannica, *Fluid*, 2011. [Online]. Available: https://www.britannica.com/science/fluid-physics.

[18] J. H. Spurk and N. Aksel, *Fluid Mechanics*, 3rd ed. Cham: Springer International Publishing, 2020, ISBN: 978-3-030-30258-0. DOI: 10.1007/978-3-030-30259-7.

[19] I. M. Cohen, P. K. Kundu, and P. S. Ayyaswamy, *Fluid Mechanics*, 4th ed. Elsevier Science and Technology, 2007, ISBN: 9780080555836.

[20] J. D. Anderson, *Fundamentals of aerodynamics*, 6th ed. New York: McGraw-Hill Education, 2017, ISBN: 978-1-259-12991-9.

[21] F. M.White, *Viscous Fluid Flow*, 3rd ed. McGraw-Hill Education, 2006, ISBN: 007-124493-X.

[22] J. Hoffman and C. Johnson, "Resolution of d'Alembert's paradox," *Journal of Mathematical Fluid Mechanics*, vol. 12, no. 3, pp. 321–334, 2010, ISSN: 14226928. DOI: 10.1007/s00021-008-0290-1.

[23] S. Glegg and W. Devenport, *Aeroacoustics of Low Mach Number Flows*. Academic Press, 2017, ISBN: 978-0-12-809651-2.

[24] C. Bailly and G. Comte-Bellot, *Turbulence*, ser. Experimental Fluid Mechanics. Cham: Springer International Publishing, 2015, ISBN: 978-3-319-16159-4. DOI: 10.1007/978-3-319-16160-0.

[25] R. E. Ecke, "From 2D to 3D in fluid turbulence: Unexpected critical transitions," *Journal of Fluid Mechanics*, vol. 828, pp. 1–4, 2017, ISSN: 14697645. DOI: 10.1017/jfm.2017.507.

[26] B. Launder and D. Spalding, "The numerical computation of turbulent flows," *Computer Methods in Applied Mechanics and Engineering*, vol. 3, no. 2, pp. 269–289, Mar. 1974, ISSN: 00457825. DOI: 10.1016/0045-7825(74)90029-2.

[27] D. C. Wilcox, *Turbulence Modelling for CFD*, 3rd ed. DCW Industries, 2006, ISBN: 9781928729082.

[28] J. C. Kok, "Resolving the Dependence on Freestream Values for the k-omega Turbulence Model," *AIAA Journal*, vol. 38, no. 7, pp. 1292–1295, Jul. 2000, ISSN: 0001-1452. DOI: 10.2514/2.1101.

[29] F. R. Menter, "Two-equation eddy-viscosity turbulence models for engineering applications," *AIAA Journal*, vol. 32, no. 8, pp. 1598–1605, Aug. 1994, ISSN: 0001-1452. DOI: 10.2514/3.12149.

[30] H. Schlichting and K. Gersten, *Boundary-Layer Theory*, 9th ed. Berlin, Heidelberg: Springer, 2017, ISBN: 978-3-662-52917-1. DOI: 10.1007/978-3-662-52919-5.

[31] tec-science. "Flow separation (boundary layer separation)." (May 2020), [Online]. Available: https://www.tec-science.com/mechanics/gases-and-liquids/flow-separation-boundary-layer-separation/ (visited on 05/14/2021).

[32] Met Office. "Beaufort wind force scale." (n.d.), [Online]. Available: https://www.metoffice.gov.uk/weather/guides/coast-and-sea/beaufort-scale (visited on 05/25/2021).

[33] Engineering ToolBox. "Air - dynamic and kinematic viscosity." (2003), [Online]. Available: https://www.engineeringtoolbox.com/air-absolute-kinematic-viscosity-d_601.html (visited on 08/31/2020).

[34] M. J. Crocker, *Handbook of Acoustics - Knovel*. John Wiley & Sons, 1998, ISBN: 978-0-471-25293-1. [Online]. Available: https://app.knovel.com/web/toc.v/cid:kpHA000023/viewerType:toc//root%7B%5C_%7Dslug:handbook-of-acoustics?kpromoter=marc.

[35] P. M. Morse and K. U. Ingård, *Theoretical Acoustics*. New York: McGraw-Hill Book Company, 1968.

[36] U. Ingard and V. K. Singhal, "Upstream and downstream sound radiation into a moving fluid," *The Journal of the Acoustical Society of America*, vol. 54, no. 5, pp. 1343–1346, Nov. 1973, ISSN: 0001-4966. DOI: 10.1121/1.1914431.

[37] A. Dowling, "Convective amplification of real simple sources," *Journal of Fluid Mechanics*, vol. 74, no. 3, pp. 529–546, 1976, ISSN: 14697645. DOI: 10.1017/S0022112076001936.

[38] E. W. Graham and B. B. Graham, "Effect of a Shear Layer on Plane Waves of Sound in a Fluid," *The Journal of the Acoustical Society of America*, vol. 46, no. 1B, pp. 169–175, 1969, ISSN: 0001-4966. DOI: 10.1121/1.1911666.

[39] K. Attenborough, "Wind and Temperature Effects on Sound Propagation," in *Springer Handbook of Acoustics*, T. D. Rossing, Ed., Springer, 2007, ch. 4.8, pp. 131–142, ISBN: 978-0-387-30446-5.

[40] L. Nijs and C. P. A. Wapenaar, "The influence of wind and temperature gradients on sound propagation, calculated with the two-way wave equation," *The Journal of the Acoustical Society of America*, vol. 87, no. 5, pp. 1987–1998, May 1990, ISSN: 0001-4966. DOI: 10.1121/1.399326.

[41] M. Hornikx, M. Dohmen, K. Conen, T. van Hooff, and B. Blocken, "The wind effect on sound propagation over urban areas: Predictions for generic urban sections," *Building and Environment*, vol. 144, pp. 519–531, Oct. 2018, ISSN: 03601323. DOI: 10.1016/j.buildenv.2018.08.041.

[42] S. C. Trikootam and M. Hornikx, "The wind effect on sound propagation over urban areas: Experimental approach with an uncontrolled sound source," *Building and Environment*, vol. 149, pp. 561–570, Feb. 2019, ISSN: 03601323. DOI: 10.1016/j.buildenv.2018.11.037.

[43] C. Weng, S. Boij, and A. Hanifi, "The attenuation of sound by turbulence in internal flows," *The Journal of the Acoustical Society of America*, vol. 133, no. 6, pp. 3764–3776, 2013, ISSN: 0001-4966. DOI: 10.1121/1.4802894.

[44] COMSOL Multiphysics, *Acoustics Module User's Guide*. 2019.

[45] A. S. Dukhin and P. J. Goetz, "Bulk viscosity and compressibility measurement using acoustic spectroscopy," *The Journal of Chemical Physics*, vol. 130, no. 12, p. 124 519, Mar. 2009, ISSN: 0021-9606. DOI: 10.1063/1.3095471.

[46] J. Gikadi, S. Föller, and T. Sattelmayer, "Impact of turbulence on the prediction of linear aeroacoustic interactions: Acoustic response of a turbulent shear layer," *Journal of Sound and Vibration*, vol. 333, no. 24, pp. 6548–6559, 2014, ISSN: 10958568. DOI: 10.1016/j.jsv.2014.06.033.

[47] R. Eklund, "Languages with pulmonic ingressive speech: updating and adding to the list," in *Fonetik*, Lund, 2015, pp. 31–34. [Online]. Available: https://www.diva-portal.org/smash/record.jsf?pid=diva2%7B%5C%%7D3A894983%7B%5C&%7Ddswid=7226.

[48] H. Fletcher, *Speech and Hearing in Communication*, J. B. Allen, Ed. The Acoustical Society of America, 1995.

[49] V. Pulkki and M. Karjalainen, *Communication Acoustics*. John Wiley & Sons, 2015, ISBN: 978-1-118-86654-2.

[50] B. Lindblom and J. Sundberg, "The Human Voice in Speech and Singing," in *Springer Handbook of Acoustics*, T. D. Rossing, Ed., Springer, 2007, ch. 16, pp. 669–712, ISBN: 978-0-387-30446-5.

[51] W. O. Olsen, "Average Speech Levels and Spectra in Various Speaking/Listening Conditions," *American Journal of Audiology*, vol. 7, no. 2, pp. 21–25, Oct. 1998, ISSN: 1059-0889. DOI: 10.1044/1059-0889(1998/012).

[52] B. F. Katz and C. D'Alessandro, "Directivity measurements of the singing voice," in *19th International Congress on Acoustics*, Madrid, Spain, 2007.

[53] P. Kocon and B. B. Monson, "Horizontal directivity patterns differ between vowels extracted from running speech," *The Journal of the Acoustical Society of America*, vol. 144, no. 1, EL7–EL12, Jul. 2018, ISSN: 0001-4966. DOI: 10.1121/1.5044508.

[54] P. Buser and M. Imbert, *Audition*. Cambridge, MA: A Bradford Book, 1992, ISBN: 0-262-02331-8.

[55] S. Reinfeldt, P. Östli, B. Håkansson, and S. Stenfelt, "Hearing one's own voice during phoneme vocalization—Transmission by air and bone conduction," *The Journal of the Acoustical Society of America*, vol. 128, no. 2, pp. 751–762, 2010, ISSN: 0001-4966. DOI: 10.1121/1.3458855.

[56] C. Johnson, *Numerical solution of partial differential equations by the finite element method*, Dover ed., ser. Dover books on mathematics. Mineola, N.Y: Dover Publications, 2009, ISBN: 978-0-486-46900-3.

[57] A. J. Davies, *The finite element method an introduction with partial differential equations*, 2nd ed. Oxford ; Oxford University Press, 2011, ISBN: 1-283-42690-0.

[58] COMSOL, *The Finite Element Method (FEM)*, 2017. [Online]. Available: https://www.comsol.com/multiphysics/finite-element-method (visited on 06/03/2021).

[59] C. Liu, *A Brief Introduction to the Weak Form*, 2014. [Online]. Available: https://www.comsol.com/blogs/brief-introduction-weak-form/ (visited on 06/03/2021).

[60] C. Wollblad, *How to Set Up a Mesh in COMSOL Multiphysics® for CFD Analyses*, 2018. [Online]. Available: https://www.comsol.com/blogs/how-to-set-up-a-mesh-in-comsol-multiphysics-for-cfd-analyses/ (visited on 06/04/2021).

[61] W. Frei, *Meshing Your Geometry: When to Use the Various Element Types*, 2013. [Online]. Available: https://www.comsol.com/blogs/meshing-your-geometry-various-element-types/ (visited on 06/04/2021).

[62] J. Gaffney, *How to Automate Meshing in Frequency Bands for Acoustic Simulations*, 2019. [Online]. Available: https://www.comsol.com/blogs/how-to-automate-meshing-in-frequency-bands-for-acoustic-simulations/.

[63] COMSOL, *COMSOL Multiphysics Reference Manual*. 2019.

[64] J. Huang, *Modeling Pressure Acoustics in COMSOL®: Video Lecture Series*, 2021. [Online]. Available: https://www.comsol.com/video/modeling-pressure-acoustics-in-comsol-video-lecture-series (visited on 06/05/2021).

[65] COMSOL Multiphysics. "Head and torso hrtf computation." (n.d.), [Online]. Available: https://www.comsol.fi/model/head-and-torso-hrtf-computation-75011 (visited on 02/11/2021).

[66] E. B. Brixen, "Microphones, High Wind and Rain," in *AES Convention 119*, New York: Audio Engineering Society, 2005. [Online]. Available: http://www.aes.org/e-lib/browse.cfm?elib=13335.

[67] C. W. Park and S. J. Lee, "Effects of free-end corner shape on flow structure around a finite cylinder," *Journal of Fluids and Structures*, vol. 19, no. 2, pp. 141–158, 2004, ISSN: 08899746. DOI: 10.1016/j.jfluidstructs.2003.12.001.

[68] E. B. Brixen and R. Hensen, "Wind Generated Noise in Microphones - An Overview - Part 1," in *AES Convention 120*, Paris: Audio Engineering Society, 2006. [Online]. Available: http://www.aes.org/e-lib/browse.cfm?elib=13439.

[69] A. Farina, "Simultaneous measurement of impulse response and distortion with a swept-sine technique," in *AES Convention 108*, Paris: Audio Engineering Society, 2000.

[70] J. Vanderkooy and S. G. Norcross, "Multitone Testing of Audio Systems," in *AES Convention 101*, Los Angeles: Audio Engineering Society, 1996. [Online]. Available: http://www.aes.org/e-lib/browse.cfm?elib=10219.

[71] E. Czerwinski, A. Voishvillo, S. Alexandrov, and A. Terekhov, "Multitone testing of sound system components – some results and conclusions. Part 1: History and theory," *Journal of the Audio Engineering Society*, vol. 49, no. 11, pp. 1011–1048, 2001, ISSN: 00047554.

[72] M. Friese, "Multitone signals with low crest factor," *IEEE Transactions on Communications*, vol. 45, no. 10, pp. 1338–1344, 1997, ISSN: 00906778. DOI: 10.1109/26.634697.

[73] R. G. Lyons, *Understanding Digital Signal Processing*, 3rd ed. Upper Saddle River, NJ: Pearson, 2010, ISBN: 9780137028450.

[74] G. Taraldsen, T. Berge, F. Haukland, B. H. Lindqvist, and H. Jonasson, "Uncertainty of decibel levels," *The Journal of the Acoustical Society of America*, vol. 138, no. 3, pp. 264–269, 2015, ISSN: 0001-4966. DOI: 10.1121/1.4929619. [Online]. Available: http://dx.doi.org/10.1121/1.4929619.

[75] J. R. Taylor, *An Introduction to Error Analysis : the Study of Uncertainties in Physical Measurements*, 2nd ed. Sausalito, CA: University Science Books, 1997, ISBN: 978-0-935702-42-2.

[76] Mathworks. "Splines in the plane." (n.d.), [Online]. Available: https://se.mathworks.com/help/curvefit/splines-in-the-plane.html (visited on 05/22/2021).

A Sample measurement results

Table A1: *Mean measured differences between **upwind** and stationary magnitude responses and their standard errors for different wind speeds at sample multitone frequencies.*

Frequency	6.3 m/s		11.7 m/s		23.3 m/s	
(Hz)	$\Delta\overline{L}$ (dB)	$\sigma_{\Delta\overline{L}}$ (dB)	$\Delta\overline{L}$ (dB)	$\sigma_{\Delta\overline{L}}$ (dB)	$\Delta\overline{L}$ (dB)	$\sigma_{\Delta\overline{L}}$ (dB)
249	-0.3	0	-0.7	0.1	–	–
308	-0.3	0	-0.7	0.1	–	–
403	-0.2	0	-0.5	0.2	-1.1	0.2
500	-0.4	0.1	-0.7	0.4	-1.8	0.2
619	-0.3	0.1	-0.7	0.5	-1.7	0.2
809	-0.2	0.1	-0.5	0.2	-1.4	0.2
1001	-0.2	0.1	-0.4	0.3	-1.2	0.1
1240	-0.2	0.1	-0.5	0.5	-1.1	0.2
1621	-0.2	0.2	-0.6	0.8	-1.6	0.2
2008	-0.1	0.3	-0.5	0.9	-1.6	0.3
2487	-0.2	0.1	-0.8	0.3	-1.2	0.2
3081	0.1	0.2	-0.5	0.1	-1.4	0.1
4026	0.1	0.2	-0.2	0.3	-1.3	0.2

Table A2: *Mean measured differences between **downwind** and stationary magnitude responses and their standard errors for different wind speeds at sample multitone frequencies.*

Frequency	6.5 m/s		12.0 m/s		23.5 m/s	
(Hz)	$\Delta\overline{L}$ (dB)	$\sigma_{\Delta\overline{L}}$ (dB)	$\Delta\overline{L}$ (dB)	$\sigma_{\Delta\overline{L}}$ (dB)	$\Delta\overline{L}$ (dB)	$\sigma_{\Delta\overline{L}}$ (dB)
249	0.3	0.1	0.9	0.1	–	–
308	0.3	0.1	0.8	0.1	–	–
403	0.2	0.1	0.6	0.1	1.9	0.2
500	0.1	0.2	0.6	0.2	2.2	0.3
619	-0.1	0.3	0.4	0.2	1.6	0.3
809	0.1	0.1	0.3	0.1	1.4	0.2
1001	0.1	0.1	0.3	0.1	1.3	0.2
1240	0.0	0.1	0.2	0.2	1.2	0.3
1621	0.0	0.3	0.1	0.3	1.3	0.7
2008	0.1	0.2	0.2	0.5	1.2	0.6
2487	-0.2	0.3	0.0	0.1	0.4	0.4
3081	0.1	0.1	0.3	0.1	1.4	0.5
4026	0.0	0.2	0.0	0.1	0.0	0.5